

REPORT DOCUMENTATION PAGE			Form Approved OMB NO. 0704-0188		
<p>The public reporting burden for this collection of information is estimated to average 1 hour per response, including the time for reviewing instructions, searching existing data sources, gathering and maintaining the data needed, and completing and reviewing the collection of information. Send comments regarding this burden estimate or any other aspect of this collection of information, including suggestions for reducing this burden, to Washington Headquarters Services, Directorate for Information Operations and Reports, 1215 Jefferson Davis Highway, Suite 1204, Arlington VA, 22202-4302. Respondents should be aware that notwithstanding any other provision of law, no person shall be subject to any penalty for failing to comply with a collection of information if it does not display a currently valid OMB control number.</p> <p>PLEASE DO NOT RETURN YOUR FORM TO THE ABOVE ADDRESS.</p>					
1. REPORT DATE (DD-MM-YYYY) 19-01-2011		2. REPORT TYPE Final Report		3. DATES COVERED (From - To) 16-Apr-2007 - 15-Oct-2010	
4. TITLE AND SUBTITLE Final Progress Report			5a. CONTRACT NUMBER W911NF-07-1-0205		
			5b. GRANT NUMBER		
			5c. PROGRAM ELEMENT NUMBER 611102		
6. AUTHORS Aristide Dogariu			5d. PROJECT NUMBER		
			5e. TASK NUMBER		
			5f. WORK UNIT NUMBER		
7. PERFORMING ORGANIZATION NAMES AND ADDRESSES University of Central Florida Office of Research University of Central Florida Orlando, FL 32826 -0150			8. PERFORMING ORGANIZATION REPORT NUMBER		
9. SPONSORING/MONITORING AGENCY NAME(S) AND ADDRESS(ES) U.S. Army Research Office P.O. Box 12211 Research Triangle Park, NC 27709-2211			10. SPONSOR/MONITOR'S ACRONYM(S) ARO		
			11. SPONSOR/MONITOR'S REPORT NUMBER(S) 52611-PH.1		
12. DISTRIBUTION AVAILABILITY STATEMENT Approved for Public Release; Distribution Unlimited					
13. SUPPLEMENTARY NOTES The views, opinions and/or findings contained in this report are those of the author(s) and should not be construed as an official Department of the Army position, policy or decision, unless so designated by other documentation.					
14. ABSTRACT The project addressed a number of fundamental aspects electromagnetic fields and their applications in inverse scattering problems. The program advanced the understanding of generation, propagation, manipulation and detection of random electromagnetic beams. The research effort comprised theoretical, numerical modeling, and experimental developments. We have demonstrated a new way of analyzing the fluctuations of scattered waves and have shown that individual members of an ensemble of interactions provides means to extract information beyond					
15. SUBJECT TERMS Coupled Dipole, Random media					
16. SECURITY CLASSIFICATION OF:			17. LIMITATION OF ABSTRACT UU	15. NUMBER OF PAGES	19a. NAME OF RESPONSIBLE PERSON Aristide Dogariu
a. REPORT UU	b. ABSTRACT UU	c. THIS PAGE UU			19b. TELEPHONE NUMBER 407-823-6839

Report Title

Final Progress Report

ABSTRACT

The project addressed a number of fundamental aspects electromagnetic fields and their applications in inverse scattering problems. The program advanced the understanding of generation, propagation, manipulation and detection of random electromagnetic beams. The research effort comprised theoretical, numerical modeling, and experimental developments. We have demonstrated a new way of analyzing the fluctuations of scattered waves and have shown that individual members of an ensemble of interactions provides means to extract information beyond that available in the ensemble average. This should be of particular interest for remote sensing procedures that rely on multiple exposures or extended time-scales in order to establish robust averages.

We have also demonstrated that, in spite of usually being considered a nuisance, media causing intricate scattering can act as efficient linear optical devices. We have shown that, upon calibration, random media can be used as polarimeters with remarkable properties.

List of papers submitted or published that acknowledge ARO support during this reporting period. List the papers, including journal references, in the following categories:

(a) Papers published in peer-reviewed journals (N/A for none)

1. S. Sukhov, D. Haefner, and A. Dogariu Coupled dipole method for modeling optical properties of large-scale random media, Phys. Rev E 77, 066709 (2008)
2. T. Kohlgraf-Owens, and A. Dogariu, "Finding the field transfer matrix of scattering media", Opt. Exp. 77, 13225 (2008)
3. J. Broky, K. M. Douglass, J. Ellis, and A. Dogariu, "Fluctuations of scattered waves: going beyond the ensemble average", Opt. Exp. 17, 10466-10471 (2009)
4. D. Haefner, S. Sukhov, and A. Dogariu, "Spin Hall effect in spherical geometry", Phys. Rev. Lett. 102, 123903 (2009)
5. D. Haefner, S. Sukhov, and A. Dogariu "Conservative and Nonconservative Torques in Optical Binding", Phys. Rev. Lett. 103, 173602 (2009)
6. D. Haefner, S. Sukhov, and A. Dogariu, "Scale-dependent anisotropic polarizability in mesoscopic structures", Phys. Rev E 81, 016609 (2010)
7. J. Broky and A. Dogariu, "Complex degree of mutual polarization in randomly scattered fields", Opt. Exp. 187, 20105 (2010)icate

Number of Papers published in peer-reviewed journals: 7.00

(b) Papers published in non-peer-reviewed journals or in conference proceedings (N/A for none)

Number of Papers published in non peer-reviewed journals: 0.00

(c) Presentations

1. S. Sukhov, D. Haefner, and A. Dogariu, Scattered intensity fluctuations for characterizing inhomogeneous media, OSA Annual Meeting, San Jose (2007)
2. D. Haefner, J. Ellis, S. Sukhov, and A. Dogariu, Determining Anisotropic Polarizability of Optically Inhomogeneous Media in near-field measurements OSA Annual meeting, San Jose 2007.
3. S. Sukhov, D. Haefner, and A. Dogariu, Scattered Intensity Fluctuations for Characterizing Inhomogeneous media, OSA Annual meeting, San Jose 2007.
4. S. Sukhov, S. Moiseev, and A. Dogariu, Metal-dielectric composites with dissipative and active components, OSA Annual Meeting, San Jose (2007)
5. D. Haefner, S. Sukhov, and A. Dogariu, "Near-Field Stochastic Scattering Polarimetry", 10th International Conference on Near-Field Optics, Buenos Aires, (2008)F
6. D. Haefner, S. Sukhov, and A. Dogariu, "Conservation of Angular Momentum In Mie Scattering", 10th International Conference on Near-Field Optics, Buenos Aires, (2008)
7. S. Sukhov, D. Haefner, and A. Dogariu, "Effective Anisotropic Polarizability Of Random Media", 10th International Conference on Near-Field Optics, Buenos Aires, (2008)
8. S. Sukhov, D. Haefner, and A. Dogariu, "Reconstructing The Local Dielectric Tensor From Near-Field Measurements", 10th International Conference on Near-Field Optics, Buenos Aires, (2008)
9. A. Dogariu, Stochastic sensing at subwavelength scales, invited lecture, University of Colorado, Boulder, (2008).
10. A. Dogariu, Variable coherence sensing, invited lecture, Duke University, (2008)
11. A. Dogariu, Variable coherence for sensing applications, invited lecture, AFRL Workshop on waves in complex media, Yountville, (2009)
12. John Broky, Jeremy Ellis, Aristide Dogariu, Identifying Non-Stationarities in Random EM fields: Are Speckles Really Disturbing?, OSA Annual Meeting, Rochester, (2008)
13. John Broky, Jeremy Ellis, Kyle Douglass, Aristide Dogariu, Statistical Fluctuations: Going Beyond the Ensemble Average, OSA Annual Meeting, Rochester, (2008)
14. David P. Haefner, Sergey Sukhov, Aristide Dogariu, Conservation of Angular Momentum in Mie Scattering, OSA Annual Meeting, Rochester, (2008)
15. David P. Haefner, Sergey Sukhov, Aristide Dogariu, Near-Field Modeling of Particle-Particle Interactions, OSA Annual Meeting, Rochester, (2008)
16. Thomas Kohlgraf-Owens, Aristide Dogariu, Disordered Media as Efficient Optical Devices, OSA Annual Meeting, Rochester, (2008)
17. David P. Haefner, Sergey Sukhov, Aristide Dogariu, Local Anisotropic Polarizability in Mesoscopic Structures, CLEO/IQEC (2009)
18. Sergey Sukhov, David P. Haefner, Girish Agarwal and Aristide Dogariu, Enhanced Birefringence of Inhomogeneous Slabs, CLEO/IQEC (2009)
19. Thomas W. Kohlgraf-Owens, Aristide Dogariu, Optimized polarimetry with massively parallel polarization sampling, SPIE Defense, Orlando (2009)
20. A. Dogariu, Optical forces and torques at nanoscales, invited lecture, Max Planck Institute for the Science of Light, Nov 2009.
21. A. Dogariu Task oriented sensing with complex waveforms, invited presentation at OSA Annual Meeting, San Jose, Oct. 2009
22. David Haefner, Sergey Sukhov, Aristide Dogariu, Nonconservative Optical Torques, CLEO/IQEC, San Jose, (2010)
23. Kyle M. Douglass, Gabriel Biener, Sergey Sukhov, Aristide Dogariu, Rotational Stochastic Resonance, CLEO/IQEC, San Jose, (2010)J₁

Number of Presentations: 23.00

Non Peer-Reviewed Conference Proceeding publications (other than abstracts):

Number of Non Peer-Reviewed Conference Proceeding publications (other than abstracts):

Peer-Reviewed Conference Proceeding publications (other than abstracts):

Number of Peer-Reviewed Conference Proceeding publications (other than abstracts):

(d) Manuscripts

Number of Manuscripts: 0.00

Patents Submitted

Patents Awarded

Awards

Graduate Students

<u>NAME</u>	<u>PERCENT SUPPORTED</u>
John Broky	0.50
David Haefner	0.70
Kyle Douglass	0.30
Thomas Kohlgraf-Owens	0.50
FTE Equivalent:	2.00
Total Number:	4

Names of Post Doctorates

<u>NAME</u>	<u>PERCENT SUPPORTED</u>
FTE Equivalent:	
Total Number:	

Names of Faculty Supported

<u>NAME</u>	<u>PERCENT SUPPORTED</u>	National Academy Member
Aristide Dogariu	0.08	No
FTE Equivalent:	0.08	
Total Number:	1	

Names of Under Graduate students supported

<u>NAME</u>	<u>PERCENT SUPPORTED</u>
FTE Equivalent:	
Total Number:	

Student Metrics

This section only applies to graduating undergraduates supported by this agreement in this reporting period

The number of undergraduates funded by this agreement who graduated during this period:

The number of undergraduates funded by this agreement who graduated during this period with a degree in science, mathematics, engineering, or technology fields:.....

The number of undergraduates funded by your agreement who graduated during this period and will continue to pursue a graduate or Ph.D. degree in science, mathematics, engineering, or technology fields:.....

Number of graduating undergraduates who achieved a 3.5 GPA to 4.0 (4.0 max scale):.....

Number of graduating undergraduates funded by a DoD funded Center of Excellence grant for Education, Research and Engineering:.....

The number of undergraduates funded by your agreement who graduated during this period and intend to work for the Department of Defense

The number of undergraduates funded by your agreement who graduated during this period and will receive scholarships or fellowships for further studies in science, mathematics, engineering or technology fields:

Names of Personnel receiving masters degrees

NAME

Total Number:

Names of personnel receiving PHDs

NAME

Total Number:

Names of other research staff

NAME

PERCENT SUPPORTED

FTE Equivalent:

Total Number:

Sub Contractors (DD882)

Inventions (DD882)

To: Richard Hammond

Subject: Final Progress Report

Contract/Grant #: W911NF0710205

PI: Aristide Dogariu

Reporting Period: 04.16.2007 - 08.31.2010

Summary

The project addressed a number of fundamental aspects electromagnetic fields and their applications in inverse scattering problems. The program advanced the understanding of generation, propagation, manipulation and detection of random electromagnetic beams. The research effort comprised theoretical, numerical modeling, and experimental developments.

In order to simulate the results of scattering from a random medium to a degree of accuracy that will reflect the statistical nature of the studied phenomenon, the coupled dipoles approximation (CDA) is a method of choice. CDA does not suffer from the important disadvantage of FDTD and FEM, namely the need to discretise space outside the medium and the need to implement suitable boundary conditions to prevent non-physical reflections from the boundaries of the computational domain. We have developed a CDA algorithm capable of dealing with different realizations of a random medium and statistical analysis of the light scattered as a result of light matter interaction.

In most cases of interest for remote sensing, the result of interaction between coherent waves and random media is scale dependent. We investigated the coherent scattering from random media both numerically and experimentally. We have developed a formalism to describe the vectorial properties of random media and, based on the scale dependent responses, we have suggested unique sensing approaches. Our findings are relevant for both material identification and the design of novel materials because we have identified a new electromagnetic interaction, which represents the scale at which the polarimetric response of a medium is most sensitive to the excitation field

We have demonstrated a new way of analyzing the fluctuations of scattered waves and have shown that individual members of an ensemble of interactions provides means to extract information beyond that available in the ensemble average. This should be of particular interest for remote sensing procedures that rely on multiple exposures or extended time-scales in order to establish robust averages.

We have also demonstrated that, in spite of usually being considered a nuisance, media causing intricate scattering can act as efficient linear optical devices. We have shown that, upon calibration, random media can be used as polarimeters with remarkable properties.

When coherent beams interact with random media, a number of polarization dependent phenomena occur. For instance, due to spin-orbit interaction, the optical wave encounter with a gradient of refractive index leads to transport of spin similar to the electronic spin Hall effect. We have demonstrated that for a wave in a pure state of polarization, the spin-orbit interaction results in a spiraling power flow that is determined by the extent of interaction. This constitutes the first demonstration that spin transport can be manipulated and enhanced in confined geometries. The results open the possibility for new functionalities for sensing devices and unique communication channels.

It has been known for quite some time that electromagnetic fields can induce conservative forces resulting from field gradients as well as nonconservative forces appearing due to radiation pressure and gradients of phase. We have uncovered a novel interplay between conservative and nonconservative forces, which constitutes a new mechanism to induce torques on spherically symmetric, optically isotropic, and lossless objects. The phenomenon can be exploited to generate torques that are fully controlled by the polarization of the excitation field. Because the torques acting on components of a material system are entirely nonconservative, the phenomenon represents a new means to extract energy from a radiation field besides the traditional dissipation mechanisms.

Certain results of this program have been included in a number of publications: two Phys Rev Lett, two Phys Rev E, and three Opt. Exp. The program has also supported a number of twenty three presentations and invited presentations at national and international scientific meetings.

1. Coupled dipole approximation for random media

The coupled dipoles approximation (CDA) is a numerical technique that discretizes a continuum volume in a finite array of polarizable point dipoles [1]. These dipoles react to the local field and, by the use of dyadic Green's function, the complete interactions between dipoles, including both the near- and far-field components, are accounted for. The polarizability of each individual dipole relates to the local dielectric properties of the medium. In modeling a near field experiment, the initial excitation is produced by an emitting dipole placed in the near field of the medium which simulates the tip of the fiber.

According to coupled dipole approximation the field at each of the dipoles can be written as the summation of both the incident field and the contributions occurring from the interaction with all the other dipoles on the lattice

$$\vec{E}(\vec{r}_j) = \vec{E}^{inc}(\vec{r}_j) + \sum_{k=1}^N \vec{E}_k^{dip}(\vec{r}_j), \quad (1)$$

where $\vec{E}_k^{dip}(\vec{r}_j)$ is the electric field radiated to the point \vec{r}_j by the k^{th} point dipole \vec{P}_k . Considering a point dipole at an arbitrary orientation and at an arbitrary location \vec{r}_k , the radiated field can be written as:

$$\vec{E}_k^{dip}(\vec{r}_j) = -[A(\vec{r}_j, \vec{r}_k)] \cdot \vec{P}_k, \quad (2)$$

where $A(\vec{r}_j, \vec{r}_k)$ is the interaction matrix accounting for both near- and far-field coupling components as a result of the dyadic Green's function. This matrix is a dense, symmetric positive definite matrix of size $3N \times 3N$ where N is the number of dipoles used. The elements of $A(\vec{r}_j, \vec{r}_k)$ can be found by:

$$A_{j,k} = \frac{\exp(ikr_{jk})}{r_{jk}} \left[k^2 (\hat{r}_{jk} \hat{r}_{jk} - I_3) + \frac{ikr_{jk} - 1}{r_{jk}^2} (3\hat{r}_{jk} \hat{r}_{jk} - I_3) \right], \quad (3)$$

where $r_{jk} \equiv |\vec{r}_j - \vec{r}_k|$ and $\hat{r}_{jk} \equiv \frac{(\vec{r}_j - \vec{r}_k)}{r_{jk}}$.

To model inhomogeneous media using CDA, dipoles with polarizabilities given by the Lorenz-Lorenz formula corresponding to the specific components were randomly distributed in a proportion according to the sample's composition. The far field coherent superposition of the dipolar contributions is recorded for specific configurations of the scattering medium and an ensemble of realizations is produced. A large number of realizations of a sample are generated and the relevant statistical information of phase, amplitude, and intensity distributions are determined.

1.2 Random Materials and CDA

In the specific case of modeling a random composite material, dipoles with the different polarizabilities are randomly distributed across the lattice in a proportion determined by the medium's composition. In our procedure, this random distribution of polarizabilities constitutes one realization of the randomly inhomogeneous medium. An ensemble of such realizations is obtained by creating a large number of independent realizations. Figure shows an example of spheres randomly distributed throughout the cubic lattice.

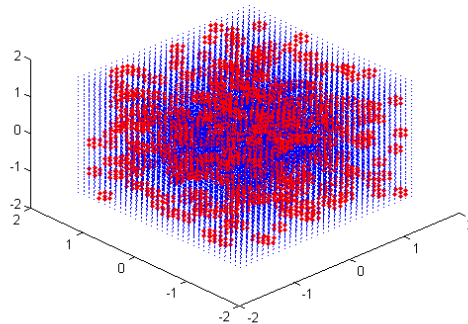


Figure 1 One realization of spheres imbedded in a host material. A sphere on a cubic lattice in this situation is modeled by 7 dipoles and is randomly distributed throughout the lattice according to the volume fraction.

The number of iterations needed to approach the solution depends on both the refractive index contrast between the different constituents, and on the initial guess at the solution. For each realization of the sample, the far-field coherent superposition of the dipolar contributions is recorded. After a large number of these realizations, an intensity distribution is created and statistically relevant information such as the optical contrast can be analyzed.

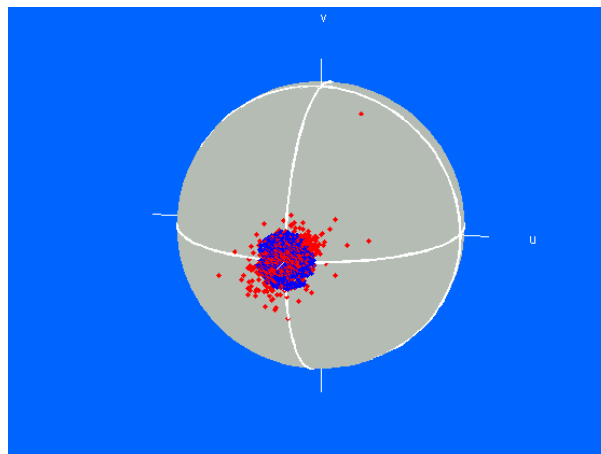


Figure 2. Distribution of states of polarization for field scattered from simulated cube of random medium. Blue points show experimental constraints, red dots show real Stokes.

1.3 Extension of CDA to infinite media

One of disadvantages of coupled dipole approximation is the rapid increase of memory requirements with increase of the number of dipoles. One of the possible ways to avoid this problem is to introduce periodic conditions for modeling geometry. For example, to study the scattering properties of infinite slab of inhomogeneous material using CDA, the modeling cube can be replicated in 2 dimensions, (x-y plane) with some periodicity specified by the initial cubes with a side dimensions d . The assumption of this extension is that this periodicity will not modify the essential properties of the scattered light.

We would like to consider the situation where we have a plane wave with some arbitrary angle of incidence on the slab of inhomogeneous material:

$$\vec{E}^{inc} = \vec{E}_o(\vec{r}_j) e^{i\vec{k}_\parallel \vec{r}_j} \quad (4)$$

According to the periodicity condition for such an excitation, we following relation should be satisfied for the field inside the slab:

$$\vec{E}(\vec{r}_j + nd\hat{x} + md\hat{y}) = \vec{E}(\vec{r}_j) e^{i\vec{k}_\parallel (nd\hat{x} + md\hat{y})} \quad (5)$$

Here \hat{x} and \hat{y} are unit vectors in the x - and y -directions, \vec{k}_\parallel is the component of wavevector parallel to the surface of the slab. The initial equation for coupled dipole approximation (1) now can be rewritten as follows:

$$\vec{E}(\vec{r}_j) = \vec{E}_o(\vec{r}_j) + \sum_{\vec{r}_j \in V_d} \bar{\alpha}_j \vec{E}(\vec{r}_j) \sum_{m,n=-\infty}^{\infty} \bar{A}(\vec{r}_j, \vec{r}_k + nd\hat{x} + md\hat{y}) e^{i\vec{k}_\parallel (nd\hat{x} + md\hat{y})} \quad (6)$$

The first summation in the right hand side of this expression is performed over all dipoles in the modeling cube. The second summation is performed over each monolayer corresponding to the repetition of each plane. Unfortunately, the lattice sums over n and m in real space does not converge. However, these lattice sums may be calculated after applying two-dimensional Fourier transformation. After proper transformations we have the following expressions for the lattice sums:

$$\begin{aligned} (z_j - z_k) &\neq 0 \\ \sum_{m,n=-\infty}^{\infty} \bar{A}(\vec{r}_j, \vec{r}_k + nd\hat{x} + md\hat{y}) e^{i\vec{k}_\parallel (\vec{r}_j + nd\hat{x} + md\hat{y})} &= \frac{i2\pi}{d^2} \sum_{p,q=-\infty}^{\infty} \frac{\vec{k}_{pq} \otimes \vec{k}_{pq} - k^2 I_3}{\kappa_{pq}} e^{(i\kappa_{pq}|z_j - z_k|)} e^{(i\vec{k}_{pq} \rho_{jk})} \\ (z_j - z_k) &= 0 \end{aligned} \quad (7)$$

In this case the sum in real space does not converge, and the sum in Fourier space diverges, as such, it is necessary to use another strategy. In this case, the sum can be written as a combination of the sum in real space and reciprocal space. The convergence is made faster by adding and subtracting and offset sum as a function of some arbitrary z value of h from the real space sum

$$\sum_{m,n=-\infty}^{\infty} \bar{A}(\vec{r}_j, \vec{r}_k + nd\hat{x} + md\hat{y}) e^{i\vec{k}_\parallel (\vec{r}_j + nd\hat{x} + md\hat{y})} = \bar{a}(\vec{k}_\parallel, h) + \left(\bar{A}(\vec{r}_j, 0) - \bar{A}(\vec{r}_j, h) \right) \quad (8)$$

Sum in inverse space is the same as the first case however now the z separation is offset from zero to be some value h :

$$\bar{a}(\vec{k}_{\parallel}, h) = \frac{i2\pi}{d^2} \sum_{p,q=-\infty}^{\infty} \frac{\vec{k}_{pq}^h \otimes \vec{k}_{pq}^h - k^2 I_3}{\kappa_{pq}^h} e^{(i\kappa_{pq} h)} e^{(i\vec{k}_{pq} \rho_{jk})} \quad (9)$$

And the sum in real space is the usual dipole interaction Green function, evaluated at $z=h$ and $z=0$

$$\bar{A}(\vec{r}_{jk}(h,0)) = \sum_{\vec{r}_{jk} \in V_d} \frac{e^{(i\kappa_{jk}^{nm})}}{r_{jk}^{nm}} \left(k^2 (\hat{r}_{jk}^{nm} \otimes \hat{r}_{jk}^{nm} - I_3) + \frac{ikr_{jk}^{nm} - 1}{r_{jk}^{nm^2}} (3\hat{r}_{jk}^{nm} \otimes \hat{r}_{jk}^{nm} - I_3) \right) e^{(i(\vec{k}_{jk})_{\parallel} (m\hat{x} + n\hat{y}))} \quad (10)$$

\otimes in formula (9) denotes the outer product,

$$\vec{k}_{pq} = (\vec{k}_{\parallel} + \vec{g}_{pq}, \text{sign}(z_j - z_k) \kappa_{pq}), \quad \vec{g}_{pq} = \frac{2\pi}{d} (p, q), \quad (11)$$

$$\kappa_{pq} = \sqrt{k^2 - (\vec{k}_{\parallel} + \vec{g}_{pq})^2}, \quad \vec{\rho}_{ij} = (\vec{r}_i - \vec{r}_j)_{\parallel}$$

where, p and q are integers.

These new expressions should allow the possibility to model a semi-infinite slab without the influence on the boundary effects. However, the new expressions are no longer symmetric with respect to the separation vector. As CDA involves solving a large dense system of equations, it often necessary to use numerical techniques that may drastically improve the efficiency of obtaining this solution. The most common technique is the use of a Fourier Transform technique and an iterative approach to the solution known as the conjugate gradient algorithm. This technique draws on the symmetries available, and as such, our new Greens function should be symmetric.

The system can become symmetric by multiplying both sides by $e^{-i\vec{k} \cdot \vec{\rho}}$ and solving a new system of equations

$$\vec{E}(\vec{r}_j) e^{-i\vec{k} \cdot \vec{\rho}} = \vec{E}_o(\vec{r}_j) e^{-i\vec{k} \cdot \vec{\rho}} + \sum_{\vec{r}_k \in V_d} \sum_{m,n=-\infty}^{\infty} \bar{A}(\vec{r}_j, \vec{r}_k + n\hat{x} + m\hat{y}) e^{i\vec{k}_{\parallel} (n\hat{x} + m\hat{y})} \bar{\alpha}_j \vec{E}(\vec{r}_k) e^{-i\vec{k} \cdot \vec{\rho}} \quad (12)$$

One feature that has not been discussed thus far is the influence of the periodicity on the scattered fields. In general, the scattering of a plane wave from a periodic structure results in diffracted orders that depend on the wavelength and the periodicity length. Figure 3 shows directions of diffracted orders for different periodicity parameters for incident field at 45° .

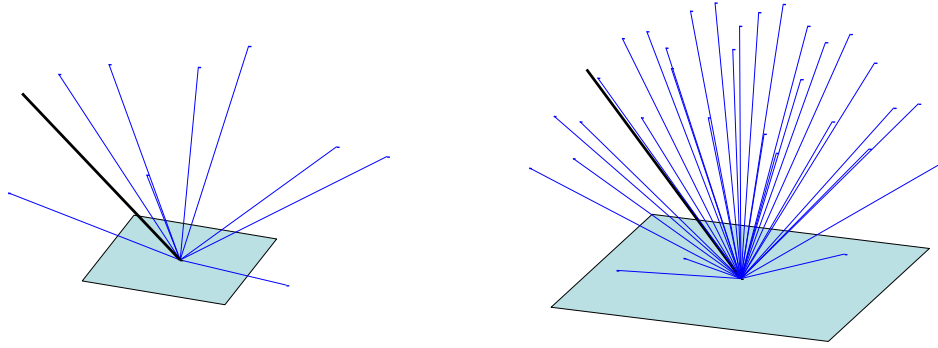


Figure 3. Directions of diffractive orders for periodicity parameter equal to $d = 1.6\lambda$ (left), $d = 3.2\lambda$ (right).

It is possible to show that in the case of homogenous material, only the 0th order diffraction occurs, corresponding to the reflected wave. In the case of inhomogeneous material, these diffracted orders do not disappear. But the presence of additional diffractive orders is not the artifact of method. Let us suppose that the periodicity approaches infinity. Then direction of diffractive orders occupy the whole space. Thus, this additional scattered light that appears in simulations could serve as some sort of measure of diffuse light.

Initial testing of the method was done in situation where the material is homogenous. For this situation, there exist analytical solutions for the field inside the slab as well as the corresponding reflection coefficients. In Figure 4 we present the comparison between the field distribution inside the slab calculated analytically according to Fresnel formulas and the results obtained using our CDA extension. The calculations demonstrate an excellent correspondence between the two approaches.

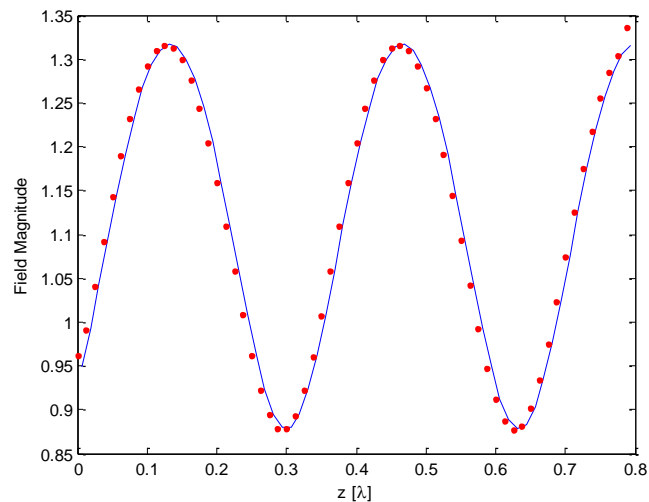


Figure 4. Electric field magnitude inside plane-parallel slab (64 dipoles in depth, total 0.8λ). Blue curve shows analytical results, red dots show the result obtained with CDA extension to infinite media.

The new method was further developed to deal with modeling large scale random media. We have demonstrated that this method can adequately describe optical properties such as specular and diffuse reflection amplitudes. The accuracy of our approach was tested on slabs with thicknesses less than the wavelength of light. We found an excellent agreement with analytical results for slabs of homogeneous media and for media containing small size inclusions. When the size of inhomogeneities increases, our numerical approach can describe phenomena for which no analytical models are available.

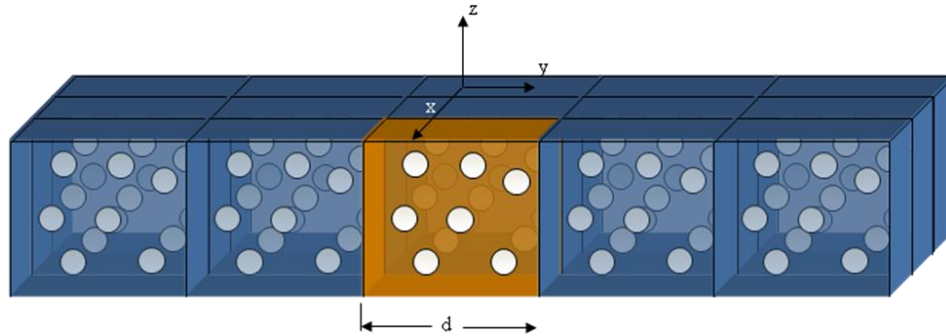


Fig. 5 Infinite slab of an inhomogeneous material modeled using CDA. The boundary effects are eliminated by replicating a random volume in 2D.

Further expansion could also address the problem of semi-infinite inhomogeneous media. However, in this case a direct extension of our approach is not possible, because the electromagnetic field in z -direction is not exactly periodic. The presence of the surface breaks the symmetry and makes the field in the surface region different from the field in the bulk. The generalization procedure should take this into account.

Another particular direction of interest is modeling roughness effects by introducing irregularities into the upper surface of the modeling cube. In the case of coupled-dipole method, media with irregular surface structure represent a particular case of inhomogeneities where some surface dipoles have zero polarizability. Thus, the formalism described above for inhomogeneous media is valid also for media with rough surfaces.

2. Scale-dependent description of inhomogeneous media

A second effort was directed at finding means to describe the effective polarizability of random media. When describing material properties, the probed scale determines the outcome. The observed material response at certain scales can depend on the local structure. In general, one can define microscopic, mesoscopic, and macroscopic regimes, but their absolute length scales will depend on the specific material characteristics.

The microscopic scale refers to the smallest volume over which the material is homogeneous; probing this scale reveals the “intrinsic” properties of the medium. The optical characteristics at the largest, macroscopic scale involve significant averaging over volumes usually much larger than characteristic scales of inhomogeneity in medium. Mesoscopic scales on the other hand, are small enough that fluctuations around the average become important and may contain additional information about structural characteristics of inhomogeneity. In this regime, the classical laws of interaction do not apply anymore.

A material is optically homogeneous when its optical responses are equivalent from micro- up to macroscopic scales. In the case of so-called inhomogeneous media, a microscopic description provides the intrinsic dielectric properties of constituents; while a description at macroscopic scales results in an effective averaging of the dielectric properties. All known effective medium theories are based on this averaging principle¹.

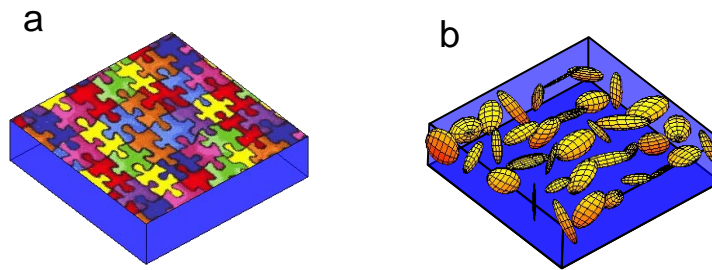


Figure 6. (a) A material system with varying optical properties over some characteristic mesoscopic length scale. (b) Conceptual model of random inhomogeneous media as that of a series of anisotropic Rayleigh scatterers.

Because materials description at mesoscopic scales involves their specific polarimetric properties, one has to go beyond conventional effective medium approaches. For instance, one can consider the mesoscopic interaction volume as being a single anisotropic Rayleigh scatterer, defined by its scattering strength, degree of anisotropy, and orientation (Fig. 6). Of course, the properties of inhomogeneous media are scale dependent and, in general, the parameters of these “anisotropic scatterers” will also depend on the mesoscopic volume considered. That means that this local anisotropy is not an intrinsic property of medium; rather, it is determined by the characteristic scale over which the measurement is performed. The notion of scale-dependent properties is a

¹ For large scale randomly inhomogeneous media, a multiscale description of the light propagation can be envisioned where the Maxwell’s equations, the transport equation, and the diffusion equation can be applied to describe the microscopic, mesoscopic, and macroscopic scale, respectively.

powerful concept, as it provides novel means to characterize inhomogeneous media². This characteristic length scale of interaction may be determined, for example, by the particles dimension if we deal with small inhomogeneous objects or by the excitation volume, as in the case of near-field optical microscopy.

2.1 Local anisotropy of inhomogeneous media

Due to their shape asymmetries, small and intrinsically homogeneous particles can acquire tensorial properties (form birefringence). Inhomogeneous objects on the other hand can have optically anisotropic properties even if their components do not have shape asymmetry. Such structurally induced anisotropy has been observed, for instance, in small spheres with eccentric inclusions. In general, collective scattering from otherwise isotropic scattering centers can manifest noticeable anisotropy in the effective polarizability.

Let us examine in detail the mesoscopic problem of an optically inhomogeneous sphere with dimensions smaller than the wavelength. The random inhomogeneities inside the sphere effectively produce an anisotropic polarizability; one method that can be applied in order to measure this anisotropic polarizability is that of stochastic scattering polarimetry (SSP). SSP will reveal the effective anisotropic polarizability of an inhomogeneous sphere if the magnitudes of the polarizability elements remain constant and polarimetric observations are performed for random orientations and different packings.

It is obvious that for some particular inhomogeneous sphere, the composite particulates may be distributed resulting in an isotropic scattering, while for others of similar properties it can be very anisotropic. To account for situations where the magnitude and orientation of the polarizability varies, a method can be outlined that fully measures the symmetric polarizability tensor of some object. Currently, in optics, one can only measure intensities; therefore a complete determination of the polarizability tensor would require three independent excitation fields and two separate polarimetric detectors. Once the complete symmetric polarizability tensor is retrieved, the diagonal form of the polarizability and the corresponding angles of rotation are found using an eigenvalue decomposition.

Using the above described method, the diagonal elements of polarizability tensor and the angles specifying its orientation can be determined for each realization of the random distribution of inclusions. The situation can be modeled using the coupled dipole approximation (CDA) described in the previous report, where dipoles with different polarizabilities α are randomly placed within the volume of the sphere. A statistically relevant number of random realizations of the sample should be performed. During every reconstruction procedure diagonal components of polarizability tensor were ordered in such a way that $a \geq b \geq c$. The probability distributions of polarizability components and orientation angles are shown in Figure 7. One can see that the distribution of angles is

² This concept has been used to describe different statistical regimes in near-field scattering from random media.

uniform. This behavior is specified by the symmetry of the problem: all the orientations of effective anisotropic polarizability of mesoscopic sphere should be equally probable. Figure 7 also shows that inhomogeneous objects indeed possess anisotropic properties at mesoscopic scales.

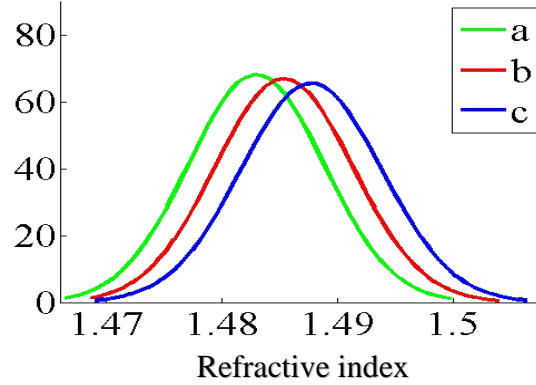


Figure 7. Probability density functions of ordered diagonal elements of polarizability tensor as obtained through the use of a sequential three independent excitations and two polarimetric detection schemes.

Let us now examine how the elements of the polarizability tensor can be measured. Of course, a complete polarimetric measurement involving three different excitations followed by detection in three different states of polarization can provide all the necessary information. However, in most scattering situations it is difficult (or not desired) to excite with three different polarizations. The question is, can some information can still be retrieved? In fact, if some assumptions about the material can be made, then the anisotropic polarizability distributions can be found by using one single polarized excitation, and a single polarimetrically measured intensity.

Due to the random nature of inhomogeneous media, there is no preferential structuring of the anisotropic polarizability tensor. That means that the main axes of polarizability tensor are oriented uniformly in space. From symmetry considerations it should also follow that the values of each of the three diagonal elements describing an anisotropic polarizability are random variables having the same probability distributions $f_a(x) = f_b(x) = f_c(x)$. If the mesoscopic region is excited by a wave linearly polarized along x , then the scattered field's magnitude along the same direction is:

$$\begin{aligned} E_x &= \nu_1(\theta, \varphi, \psi)a + \nu_2(\theta, \varphi, \psi)b + \nu_3(\theta, \varphi, \psi)c, \\ \nu_1(\theta, \varphi, \psi) + \nu_2(\theta, \varphi, \psi) + \nu_3(\theta, \varphi, \psi) &= 1, \end{aligned} \quad (13)$$

where the functions ν_1 , ν_2 and ν_3 describe the orientation of the anisotropic polarizability and are functions of the random rotations θ , φ , and ψ . It is possible to show that the random variables ν_1 , ν_2 and ν_3 have the same probability distribution functions that can be described by function

$$f_{v_1}(x) = f_{v_2}(x) = f_{v_3}(x) = \frac{1}{2\sqrt{x}}, \quad x \in [0, 1]. \quad (14)$$

However, these variables are not independent, and their joint distribution may be found to be

$$f_{v_1 v_2}(v_1, v_2) = \frac{1}{8} \left(\frac{1}{\sqrt{v_1 v_2}} + \frac{1}{\sqrt{v_1(1-v_2)}} + \frac{1}{\sqrt{(1-v_1)v_2}} - \frac{1}{\sqrt{(1-v_1)(1-v_2)}} \right). \quad (15)$$

Solving Eq. (13) for unknown PDFs $f_a(x)$, $f_b(x)$, $f_c(x)$ by using measured PDF of x-polarized electric field and then using the order statistics allows recovering the PDFs of diagonal polarizability components. The distributions of the ordered diagonal tensor elements $f_{x^{(k)}}(x)$ ($k=1,2,3$), can be inferred from the original probability distribution function $f(x)$ and the cumulative distribution function $F(x)$

$$f_{x^{(k)}}(x) = \frac{n!}{(k-1)!(n-k)!} F(x)^{k-1} (1-F(x))^{n-k} f(x), \quad n=3. \quad (16)$$

For example, applying such ordered statistics constraint to a Gaussian distribution with mean μ and standard deviation σ leads to three other ‘‘Gaussian like’’ distributions with means μ and $\mu \pm 3\sigma/(2\sqrt{\pi})$. This ordering allows us to recover the three distributions of the diagonal elements of the polarizability, reducing the demand on the measurement: single excitation polarization and single co-polarized measurement.

Our CDA simulations show that PDFs of a , b , and c for random media in many cases may be described by Gaussian distribution. Therefore, one can write:

$$f_a(a) = f_b(b) = f_c(c) = \frac{1}{\sqrt{2\pi}\sigma_\alpha} \exp\left(\frac{-(\alpha - \mu_\alpha)^2}{2\sigma_\alpha^2}\right). \quad (17)$$

Resulting co-polarized intensity distributions are also in many cases Gaussian. Using the assumptions about Gaussian form of PDFs, we can solve numerically Eq. (13) and find a relation between the moments of the scattered intensity distribution $p(|E_x|^2)$ and the moments of the Gaussian distribution of polarizability elements:

$$I_\mu^x = \mu_\alpha^2 + \frac{2}{3}\sigma_\alpha^2, \quad I_\sigma^x = \frac{5\sqrt{\pi}}{6}\mu_\alpha\sigma_\alpha + \frac{3}{4\pi}\sigma_\alpha^2. \quad (18)$$

These expressions are found from the assumptions that refractive index of components of inhomogeneous media is bounded (usually between 1 and 3). It follows that the possible variations of both mean of intensity and standard deviation are also limited. Thus, the functions $I_\mu^x = f_\mu(\mu_\alpha, \sigma_\alpha)$, $I_\sigma^x = f_\sigma(\mu_\alpha, \sigma_\alpha)$ can be decomposed into series with respect to variables μ_α , σ_α . It seems that a decomposition up to the second order produce very good results as illustrated in Figs 8 and 9 where two media are considered that have

the same effective properties (same effective refractive index) but different local morphologies as can be seen. The set of different PDF's for polarizability elements are different as observed in Figure 9 indicating that a polarimetric measurement can actually discriminate between these two media.

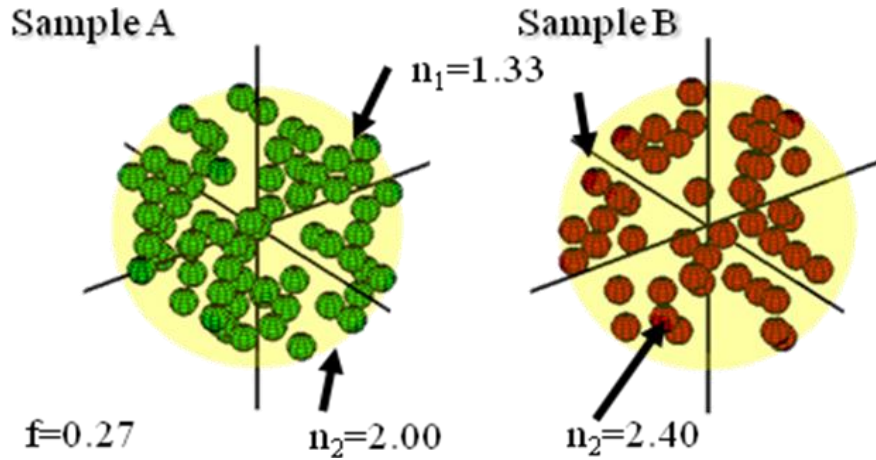


Figure 8. Example of two random media having the same effective refractive index as estimated from the Bruggeman's effective medium theory.

$$f_1 \frac{n_1 - n_{eff}}{n_1 + n_{eff}} + f_2 \frac{n_2 - n_{eff}}{n_2 + n_{eff}} = 0$$

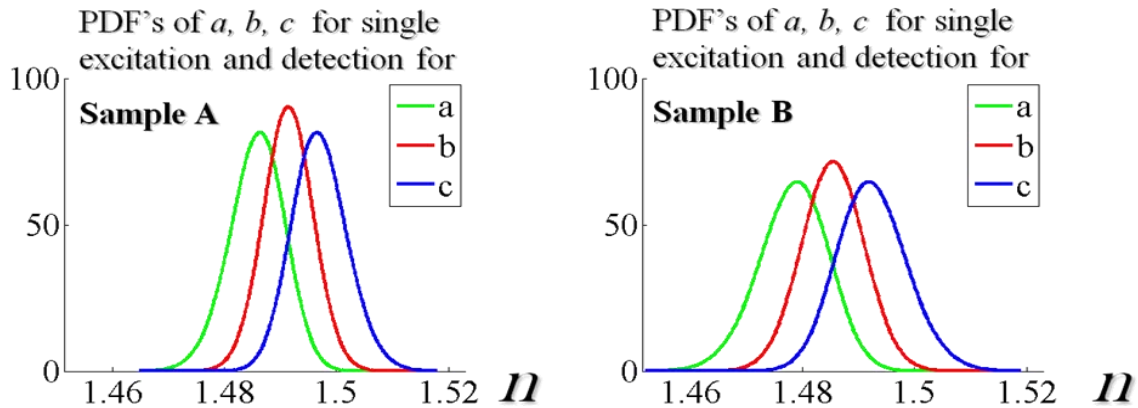


Figure 9. Probability density functions of ordered diagonal elements of polarizability tensors for samples A and B in Fig. 8 as obtained through the use a single polarimetric excitation.

2.2 Scale dependent local anisotropic polarizability

To quantitatively characterize the local anisotropic polarizability (LAP), we introduce an anisotropy factor defined as the contrast calculated for diagonal components of polarizability tensor α

$$\Delta = \frac{\sqrt{3\text{Tr}(\alpha^2) - \text{Tr}(\alpha)^2}}{\text{Tr}(\alpha)} = \sqrt{2} \frac{\sqrt{\alpha_a(\alpha_a - \alpha_b) + \alpha_b(\alpha_b - \alpha_c) + \alpha_c(\alpha_c - \alpha_a)}}{\alpha_a + \alpha_b + \alpha_c}, \quad (19)$$

where Tr denotes the trace of tensor α . Note that, in the past, other definitions have been used for such anisotropy factor. In Ref. [Error! Bookmark not defined.] for instance, an anisotropy factor S was defined as the variance of depolarization factors

$$\hat{v}(\mathbf{r}) = \frac{1}{3} \hat{I} - \int_V \hat{G}_0(\mathbf{r}, \mathbf{r}') d^3 r'. \quad \text{Here } \hat{G}_0(\mathbf{r}, \mathbf{r}') \text{ is the regular part of the quasistatic}$$

free-space dyadic Green's function for electric field, \hat{I} is the unity tensor. In this designation, the local anisotropy factor cannot depend on the excitation volume and, moreover, its locality can be violated in 3D random composites without structural self-similarity, i.e. in nonfractal composites that are of interest here.. The definition of Δ in Eq. (19) is most appropriate for our discussion, which focuses on describing the form anisotropy and not necessarily on the absolute magnitude of a specific dipole moment.

Using the definition in Eq. (19), the anisotropy factor Δ was calculated for every realization of the localized inhomogeneous volume. Of course, an averaged Δ can then be calculated from the recovered ensemble of values of this parameter. The average anisotropy factors calculated for the two materials illustrated in Fig. 8 are $9.2 \cdot 10^{-3}$ and $13.2 \cdot 10^{-3}$, respectively. The 30% difference clearly demonstrates that LAP is a parameter that can be used to quantify differences between macroscopically similar media.

In the preceding discussion, LAP was examined over one single length scale. This situation corresponds to fixed volume of light-matter interaction imposed by the measurement procedure. In case of the two different media presented in Figure 8, the differences will, of course, diminish as this volume of interaction increases; the two different optical responses will converge toward the same macroscopic value corresponding to an isotropic polarizability tensor. The rate of this convergence however may be different depending on the specific structural morphology.

We will turn now our attention to LAP's dependence on the volume of interaction. We have repeated the previous analysis for spheres of different radii R and the results are presented in Figure 10 where we compare the anisotropy factor Δ for the case of two different sizes of spherical inclusions randomly distributed within probing volume of different sizes. The main observation is that Δ always attains a maximum that defines a new length scale characterizing the electromagnetic interaction. This maximum anisotropy length (MAL) represents the length scale over which the response of inhomogeneous medium is most sensitive to the polarization (vector) properties of the excitation field. In other words, it is at this scale that, in average, the depolarization of

light during scattering occurs more effectively. Along with scattering mean free path and transport mean free path that describe the way the energy is transferred, MAL represents another interaction-specific length scale that characterizes the propagation of polarized fields through random media.

At length scales smaller than MAL, the local polarizability becomes isotropic with Δ tending to zero as the probing volume decreases. At larger scales, the macroscopic behavior is gradually approached leading again to an effectively isotropic scattering volume with $\Delta = 0$.

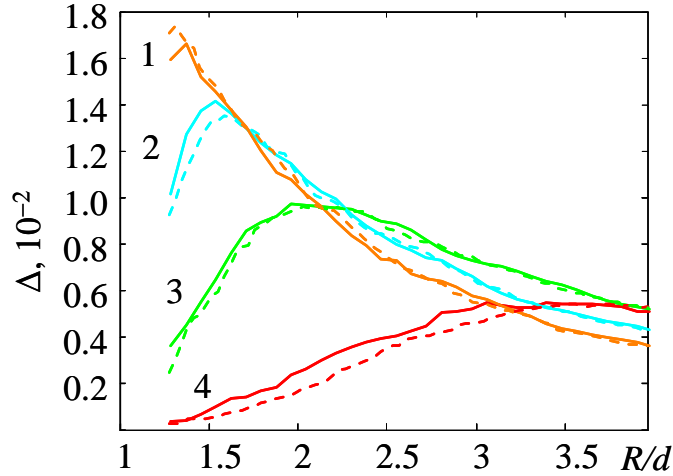


Figure 10. Effective anisotropy factor Δ as a function of excitation volume R normalized by inclusion diameter d for spherical inclusions with a refractive index of 1.5 randomly distributed in vacuum. The continuous lines correspond to inclusions with diameter $\lambda/32$ while the dashed lines correspond to inclusions of diameter $\lambda/64$. Curves 1 to 4 correspond to volume fractions of inclusions of 0.3, 0.2, 0.1, and 0.025, respectively.

As can be seen in Figure 10, the values of the anisotropy factor appear to be independent of the size of inhomogeneities. This happens, because, in our example, the interaction inside the inhomogeneous volume considered is mostly within the electrostatic regime. Therefore, the behavior of Δ does not depend on the wavelength and is fully scalable with inclusions' dimensions. Also noticeable in Figure 10 is the faster decay of Δ for higher volume fractions of inclusions inside the sphere of interaction. This can also be easily explained by realizing that, for a given excitation volume, the larger number of inclusions corresponding to a higher volume fraction represents in fact a more isotropic medium.

In the particular case when the spherical inclusions can be considered as packed hard spheres, we found that MAL has a simple interpretation. As illustrated in 11, in this case MAL defines the volume containing, in average, three inclusions. Note that three inclusions represent the minimum number of particles necessary to form a fully anisotropic scatterer. Thus, the statistical averaging for scatterers containing more than three inclusions results in a gradual decrease of the anisotropy factor.

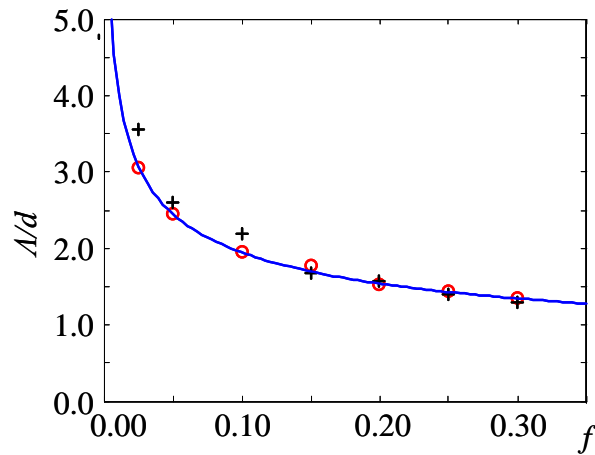


Figure 11. Maximum anisotropy length (Λ) normalized by the diameter of inclusions d versus the volume fraction of inclusions f . Open circles and crosses represent MAL values corresponding to inhomogeneous media with inclusions of diameters of $\lambda/64$, $\lambda/32$ respectively. The solid line corresponds to the volume containing on average 3 inclusions.

Of course, the other factors determining the optical response of a composite medium are the intrinsic properties of the components. It is expected that, in general, higher anisotropy factors will characterize materials with increasing dielectric contrasts. This is evident in

Figure 12 where we plot the value of the maximum anisotropy Δ_{\max} as a function of dielectric contrast of inclusions. The calculations also demonstrate that the values of Δ_{\max} simply scale with the magnitudes of dielectric functions of components indicating that the Δ_{\max} behavior is determined only by the material's structure and not by its composition.

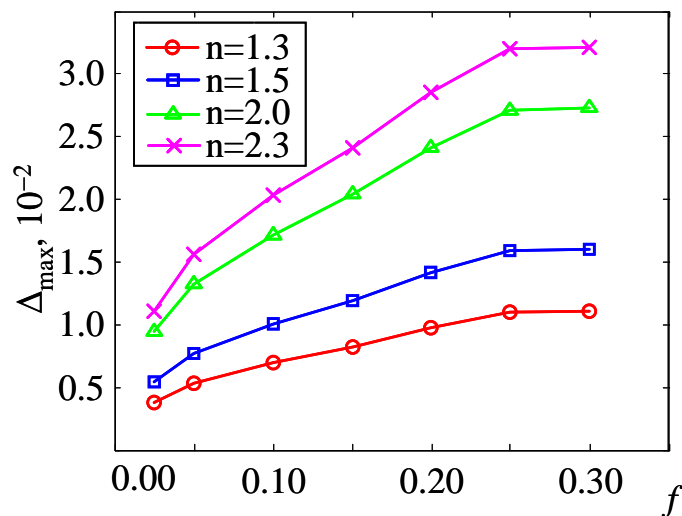


Figure 12. Maximum of anisotropy factor Δ_{\max} as a function of volume fraction f of inclusions with 50nm in diameter and having different refractive index contrasts.

To conclude, we have demonstrated that at mesoscopic scales, the optical response of random media consisting of optically isotropic components may be interpreted in terms of local anisotropic polarizabilities (LAP). At mesoscopic scales, different materials can be characterized by their specific anisotropic polarizabilities even though they may have similar effective dielectric permittivities when described in terms of an effective medium approach.

We have also shown that material properties at mesoscopic scales depend on the volume of interaction, in this respect, LAP is an attribute of the electromagnetic field-matter interaction. However, a characteristic length scale, maximum anisotropy length (MAL), exists at which the degree of local anisotropy Δ reaches its maximum. At this scale the inhomogeneous materials are most sensitive to the polarization of incident light. Thus, electromagnetic wave interaction on this scale length results in the maximal depolarization. Along with other characteristics length scales such as the scattering mean free path, the value of MAL reflects essential intrinsic properties of random media.

There are, of course, different means for characterizing the local optical properties of inhomogeneous media. For instance, the scalar contrast of scattered intensities measures the relative variations of the scattering cross-section within the interaction volume. When this volume increases, the scattered intensity variations decay monotonically to zero with a rate depending on the medium's properties. In this case however, only asymptotic scales can be determined which may affect the specificity. MAL on the other hand is not only derived from a tensorial feature of the material but it is also a local property. Its value is a basic characteristic of material's morphology.

Our findings are relevant to the design of novel materials because this new electromagnetic interaction scale represents the material scale at which the polarimetric response of a medium is most sensitive to the excitation field.

3. Field transfer matrix of scattering media

Multiple scattering is typically considered to degrade the information in a beam propagating through a random medium. For temporally coherent radiation propagating through an optically thick medium, the light scattered out of the medium will produce an interference pattern with alternating bright and dark regions known as speckles. A speckle pattern having a negative exponential intensity distribution is called fully developed and obeys Gaussian field statistics. Since the field distribution is a Gaussian random variable, it was thought to contain neither information about the underlying scattering medium nor information about the beam incident on the medium.

We investigated a new approach to recovering information from a speckle pattern that does not rely on ensemble averaging or assumptions about the underlying field statistics. We have actually measured the components of the field transfer matrix across a particular output plane. In a proof of concept demonstration, we show successful recovery of the polarization state of an unknown beam from the speckle pattern it produces. Our technique is a deterministic procedure performed simultaneously in many different spatial locations. Because the technique does not rely on any assumptions about the statistics of the field distribution and because it is carried out by point operations rather than image correlations, it can be used in regimes ranging from no scattering to high-order multiple scattering.

Consider a linear, multiply scattering medium illuminated by polarized light. The field will undergo many series of scattering events before emerging from the medium. In a particular series, the field after the first scattering event at \mathbf{r}_1 that illuminates the second scatterer at position \mathbf{r}_2 may be expressed as

$$\mathbf{E}(\mathbf{r}_2)_{scat,1} = \bar{\mathbf{a}}(\mathbf{r}_2, \mathbf{r}_1) \mathbf{E}(\mathbf{r}_1)_{inc} \quad (20)$$

where $\bar{\mathbf{a}}$ is a complex tensor that expresses the magnitude and phase of the coupling between incident and scattered field components. It also includes transferring the scattered field to the point \mathbf{r}_2 . Now, replacing \mathbf{E}_{inc} with $\mathbf{E}_{scat,1}$ and $\bar{\mathbf{a}}(\mathbf{r}_2, \mathbf{r}_1)$ with $\bar{\mathbf{a}}(\mathbf{r}_3, \mathbf{r}_2)$, we obtain the field at position \mathbf{r}_3 on the third scatterer. This process can be continued until the field reaches the detector at position \mathbf{r} to obtain the contribution of a particular scattering path to the field at the detector:

$$\mathbf{E}(\mathbf{r})_{det} = \left[\prod_i \bar{\mathbf{a}}(\mathbf{r}_{i+1}, \mathbf{r}_i) \right] \mathbf{E}(\mathbf{r}_1)_{inc} = \bar{\mathbf{a}}(\mathbf{r}, \mathbf{r}_1)_{eff} \mathbf{E}(\mathbf{r}_1)_{inc} \quad (21)$$

In this particular decomposition the scattering matrix that relates the input and output field contains information about the propagation from \mathbf{r}_i to \mathbf{r}_{i+1} as well as information about the scattering event at \mathbf{r}_i . Since we are interested in the transfer of the field through the medium, not in the particular details of how the transfer occurs, the mixing of scattering and propagation information is not important.

Furthermore, there are many scattering paths connecting the illuminated points on the front surface of a multiply scattering medium to each detection point after the medium as shown in Fig. 13. If the scattering path lengths are shorter than the coherence length of the illuminating radiation, the scattering process will not depolarize the output light; it

will only change the radiation's state of polarization. The resulting field at any detection point due to a particular input point is simply the coherent summation of the outputs of each of the different paths starting at the illuminated point on the front surface and ending at the detection point. Also shown in Fig. 13 are three random walks on the Poincare sphere that begin in the same polarization state (chosen here to be circular). However, since they interact with different configurations of the scattering medium, they arrive at the detector in different states of polarization, denoted by the large dots of the appropriate color. The total field at the detector is the coherent sum of the different paths and is in the state of polarization marked by a white dot labeled "detected" on the Poincare sphere. Thus, the resulting field, neglecting time dependence, at a point \mathbf{r} due to all illuminated input points can be written as

$$\mathbf{E}(\mathbf{r})_{total} = \sum_n \sum_{eff} \bar{\alpha}(\mathbf{r}, \mathbf{r}_n)_{eff} \mathbf{E}(\mathbf{r}_n)_{inc} = \sum_n \tilde{\alpha}(\mathbf{r}, \mathbf{r}_n) \mathbf{E}(\mathbf{r}_n)_{inc} = \tilde{\alpha}(\mathbf{r}) \hat{\mathbf{e}}_{inc} \quad (22)$$

The normalized input field, $\hat{\mathbf{e}}_{inc}$, can be factored out of the sum so long as its polarization is spatially constant, and we can express the resulting output field in terms of a single transfer matrix, $\tilde{\alpha}(\mathbf{r})$, which subsumes the intensity profile of the illumination. For a given experimental geometry and illumination source, $\tilde{\alpha}(\mathbf{r})$ is only a function of detector location; however, if the spatial intensity profile of the illumination is modified, $\tilde{\alpha}(\mathbf{r})$ will change as well because the intensity profile acts as a weighting function for the contribution of each scattering path. The tilded quantities represent the only measurable parameters of the scattering material because it is not practically possible to separate the contributions of individual paths from the detected intensity. It is also important to note that the illuminated points can have an arbitrary spatial extent and spatial intensity profile on the random scattering medium as long as the scattering paths remain coherent with one another.

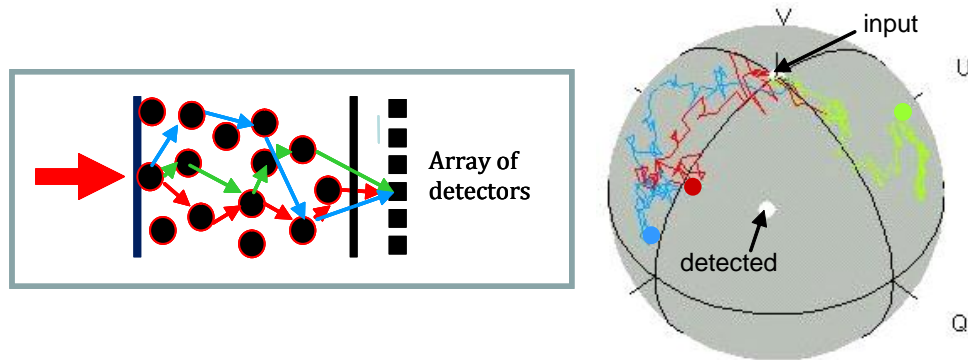


Fig. 13. Random walks through a static random medium and their resulting change in polarization state.

The problem of determining the elements of the transfer matrix to a given point in the detection plane does not depend on the precise nature of the process that produced the output field and thus applies to all scattering regimes. In general, $\tilde{\alpha}$ has nine elements with eighteen unknowns: nine coupling magnitudes and nine phases. Because the scattering is not isotropic, $\tilde{\alpha}$ depends on the direction of propagation of the incident light, and it is difficult to measure the full transfer matrix for an arbitrary geometry. However,

if the scattering medium is surrounded by an isotropic medium, the electric field of the illumination is confined to a plane and can be decomposed into two orthogonal polarization states with a phase between them. If the scattered fields are allowed to propagate away from the scattering medium before detection, they can also be decomposed into two orthogonal polarization states and a phase term. In this situation, the transfer matrix has only four elements consisting of eight unknowns, which can be determined by illuminating the scattering medium with appropriately polarized light. Moreover, we can choose one of the elements of the transfer matrix to be real since we cannot measure absolute phase at a point and only compare the intensities between points. Additional simplifications can be introduced by realizing that it is not necessary to characterize all seven of the remaining unknowns simultaneously. If a polarizer oriented along the x-axis is placed between the scattering medium and the detector, $\tilde{\alpha}_{21} = \tilde{\alpha}_{22} = 0$, and there are only three unknowns that need to be characterized. The detected intensity at point \mathbf{r} is then given by

$$I(\mathbf{r}) = [\tilde{\alpha}_{11}(\mathbf{r})E_x]^2 + [\tilde{\alpha}_{12}(\mathbf{r})E_y]^2 + 2\tilde{\alpha}_{11}(\mathbf{r})\tilde{\alpha}_{12}(\mathbf{r})E_xE_y \cos[\theta + \tilde{\phi}(\mathbf{r})], \quad (23)$$

where θ is the phase between the x and y components of the incident field, and E_x and E_y are their respective magnitudes. In Eq. (23), $\tilde{\phi}$ is the phase introduced by the coupling of E_y into a scattered x polarized field, and $\tilde{\alpha}_{11}$ and $\tilde{\alpha}_{12}$ are the magnitudes of the coupling of the incident x and y polarized fields, respectively, into scattered fields polarized along x. The polarization of the scattered field and the elements of $\tilde{\alpha}$ measured are determined by the orientation of the final polarizer.

3.1 Calibration procedure

The procedure for recovering an unknown incident state of polarization comprises three main steps:

- measuring the transfer matrix for many points in the detection plane,
- selecting unique field combinations or transfer matrices, and
- solving Eq. (10) for the incident field components using the transfer matrices.

First, the needed components of the transfer matrix corresponding to each detector point are determined via a calibration with known fields. To determine the magnitudes of the elements of the transfer matrix and eliminate the sign ambiguity in the argument of the cosine in Eq. (10), we use four calibration states. The relative spatial intensity profiles of the unknown source and the calibration source should be the same since the intensity profile of the illumination weights the contribution of each scattering path to the detected intensity.

A fully polarized field is characterized by three different parameters, and, as with the transfer matrix elements, at least three independent combinations of the incident field are needed to completely determine its polarization state. For a static system, each point in the detection plane sees a particular transformation of the input field resulting from the combination of the scattering paths that end at that point. Thus, determining the parameters of a fully polarized field requires that the intensity be measured at three or

more points with independent transfer matrices. As a result, the detection system must resolve at least three speckles.

As an example, the use of a particular combination of detectors is illustrated in Fig. 14. The axes of this representation of transfer matrices are defined in a manner analogous to the Poincare sphere with the elements of the transfer matrices at a particular point taking the place of the input field components that they couple

$$\begin{aligned}\Delta &= (\tilde{\alpha}_{11}^2 - \tilde{\alpha}_{12}^2) / (\tilde{\alpha}_{11}^2 + \tilde{\alpha}_{12}^2) \\ \sigma &= 2\tilde{\alpha}_{11}\tilde{\alpha}_{12} \cos(\tilde{\phi}) / (\tilde{\alpha}_{11}^2 + \tilde{\alpha}_{12}^2) \\ \phi &= 2\tilde{\alpha}_{11}\tilde{\alpha}_{12} \sin(\tilde{\phi}) / (\tilde{\alpha}_{11}^2 + \tilde{\alpha}_{12}^2)\end{aligned}\quad (24)$$

The points shown in blue have a transfer matrix of $\tilde{\alpha}_{11} \neq 0$ and $\tilde{\alpha}_{12} \approx 0$, while the points shown in green have a transfer matrix of $\tilde{\alpha}_{11} \approx 0$ and $\tilde{\alpha}_{12} \neq 0$. Because the output points represented by the blue and green areas couple only one of the two input field components, they measure the x and y components of the unknown field. The points shown in red on the other hand have $\tilde{\alpha}_{11} \approx \tilde{\alpha}_{12}$ and contain the information about the phase of the unknown field because both of the input field components are coupled into the measured intensity.

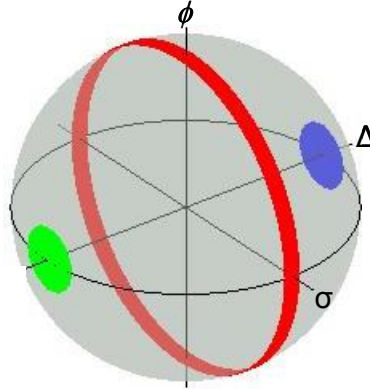


Fig. 14. Example of groups of transfer matrices that can be used to recover an unknown incident field.

Since there is no reason to select any particular group of independent detection points, it is possible to form many different groups and then perform a statistical analysis on the recovered fields rather than relying on the result of a single combination. Note that a medium with transfer matrices covering only a small portion of the sphere may not be used to fully analyze *any unknown field* from its speckle pattern simply because the medium does not produce a sufficient number of independent combinations of the field.

Finally, for the selected groups of transfer matrices as illustrated in Fig. 2, the unknown field parameters, E_x , E_y , and θ , are determined by solving the following system of equations for each group of detectors

$$\begin{aligned}I(\mathbf{r}_1) &= [\tilde{\alpha}_{11}(\mathbf{r}_1)E_x]^2 \\ I(\mathbf{r}_2) &= [\tilde{\alpha}_{12}(\mathbf{r}_2)E_y]^2 \\ I(\mathbf{r}_3) &= [\tilde{\alpha}_{11}(\mathbf{r}_3)E_x]^2 + [\tilde{\alpha}_{12}(\mathbf{r}_3)E_y]^2 + 2\tilde{\alpha}_{11}(\mathbf{r}_3)\tilde{\alpha}_{12}(\mathbf{r}_3)E_xE_y \cos[\theta + \tilde{\phi}(\mathbf{r}_3)]\end{aligned}\quad (25)$$

where all of the transfer matrix elements are known from the calibration process and where \mathbf{r}_i denotes the location of the point in the detection plane rather than the location of a scatterer.

3.2 Proof of concept demonstration

In order to demonstrate that our procedure is valid across all scattering regimes, we measured transfer matrices for the extreme cases of deterministic, single scatterers and a heavy multiple scatterer. For the single scatterers, the measured transfer matrices can be qualitatively compared to the expected values using the spherical representation from Fig. 14. On the other hand, since the multiply scattering medium produces many diverse mixings of the incident field, it is difficult to assess the capability of our procedure by direct examination of the measured transfer matrices. In this case, we will use the transfer matrices to recover the states of polarization of plane waves in order to show our procedure works even in a regime of heavy multiple scattering.

In our experiment, a laser beam with a controlled state of polarization was incident on the scattering medium and the speckle pattern resulting from its transmission through the medium was recorded by a CCD camera. A polarizer with a fixed orientation was placed in front of the detector to simplify the analysis as explained before. The speckles produced by the multiply scattering medium were approximately five pixels across on the CCD and each measurement sampled a few thousand speckles.

Figure 15 illustrates the measured transfer matrices for a polarizer, a quarter-wave plate, and a multiply scattering medium. The multiply scattering medium is a composite dielectric material with a thickness of $100\mu\text{m}$ and characterized by a transport mean free path of $10\mu\text{m}$. Figures (a) and (b) show measurements from a polarizer oriented at approximately $\pm 45^\circ$ and a quarter-wave plate rotated in 15° increments from 0° to 90° . From linear optics theory, we expect a polarizer oriented at 45° and 135° to have equal coupling strengths through the final polarizer for both incident x and y field components. Also, when the polarizer is oriented at 45° , the transmitted field components will be in phase, and when it is oriented at 135° , the transmitted field components should have a π phase difference between them. In (a) we see comparable coupling of the orthogonal field components, although there is a slight misalignment of the polarizer, and rotating the polarizer from 45° to 135° introduces a π phase shift between the elements of the transfer matrix as expected. In (b), the green line denotes the path that the transfer matrix of a quarter-wave plate should follow on the sphere as the wave plate is rotated through 90° , and the labeled groups of points are the measured transfer matrices for a quarter-wave plate in the indicated orientations. In both cases the measured transfer matrix elements show behavior consistent with what was expected and demonstrate the ability of our process to analyze deterministic single scatterers.

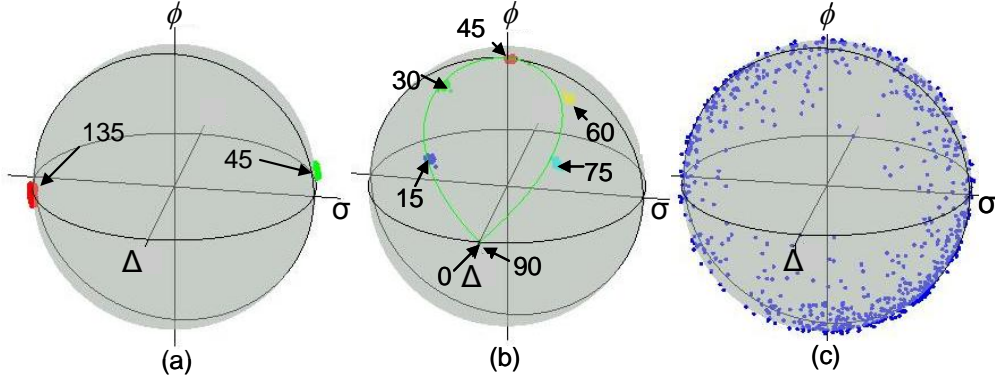


Fig. 15. Effective transfer matrices measured for (a) A polarizer oriented at roughly 45° and 135° . (b) A quarter-wave plate rotated by 90° in 15° increments. (c) A multiply scattering solid sample.

In Fig. 15(c) we present a subset of the measured transfer matrices for the multiply scattering sample. For a truly random medium, we would expect the measured transfer matrices to uniformly cover the sphere of possible matrices; however, because of numerical instabilities involving calculations with small numbers, the points in a ring around Δ axis of the sphere are rejected by our processing algorithm. Near the axis, either $\tilde{\alpha}_{11} \gg \tilde{\alpha}_{12}$ or $\tilde{\alpha}_{11} \ll \tilde{\alpha}_{12}$, and the smaller of the two can be approximated as 0 so that transfer matrices very close to the Δ axis are moved onto the axis. Also, there seems to be some clustering of the points near $\phi = -1$. Even though the transfer matrices are not uniformly distributed on the sphere, our measurements show that the sample produces a sufficiently large number of substantially different mixings of the incident field. This is the only requirement for recovering the state of polarization of the incident field.

Since the medium exemplified in Fig. 15(c) is in a regime of multiple scattering, it is difficult to assess the accuracy of the transfer matrix measurement by viewing of the matrices using this spherical representation. However, one can still examine their accuracy by using the determined matrices to infer the polarization states of different beams illuminating the medium. Fig. 16 shows typical experimental results for a $+45$ degree linear polarization and an elliptical input state, represented by the blue dots. The white dots denote the polarization states recovered by different pixel groups, and the red dots represent the geometric centers of the white data points.

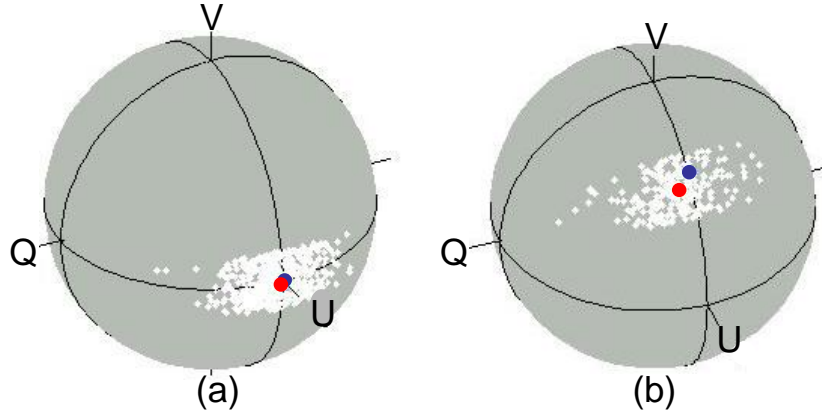


Fig. 16. Poincare sphere representations of the polarization states recovered by individual pixel groups (white dots), the geometric centers of the clouds of white points projected onto the surfaces of the spheres (red dots), and the expected polarization states (blue dots).

The experimental data shown above subtend a solid angle of approximately 0.158 steradians. The spread in the states recovered by the different detector combinations can be mitigated to a large extent by averaging the results of many combinations. The averaging can be done well because transfer matrices are measured for a large number of detectors. In order to quantify the error in the recovered polarization state, we can compare the normalized Stokes vector of the recovered field to that of the incident field. In (a) we input a Stokes vector of $(0, 1, 0)$ and measured $(0.018, 0.9997, 0.014)$, and in (b) we input $(0, 0.643, 0.766)$ and measured $(0.067, 0.638, 0.764)$. As can be seen, the recovered Stokes vector components do not deviate by more than 1% from their expected value.

We have also simulated our experiment to study the effects of the detector selection criteria and detector noise on the measured field transfer matrices. We choose $\tilde{\alpha}_{11}$ and $\tilde{\alpha}_{12}$ randomly distributed uniformly between 0 and 1 and $\tilde{\phi}_{12}$ to be randomly distributed uniformly between 0 and 2π . The magnitudes of the coupling matrices were then scaled so that the resulting calculated intensity distribution was similar to the actual data for unit strength electric field inputs. Gaussian white noise with a signal to noise ratio of 34 was then added to the intensity image to simulate the detector noise in a real measurement. Speckle images were generated for both the calibration and test states and processed using the same code as the experimental data. Our simulations indicate that the most significant source of error in the data collection and processing is the noise in the detector itself. For simulated data with no noise, the solid angle covered by the measurement data on the Poincare sphere (white dots in Fig. 4) is approximately 0.013 steradians. When noise comparable to the noise of the detector used in the experiment is added to the simulated data before processing, the spread of the recovered states increases to 0.048 steradians. The remaining error is likely due to mechanical instabilities in the experiment.

In summary, we have demonstrated that the field transfer matrices of a system can be practically measured for specific geometries. In doing so, no assumptions about the statistics of the random field and no specific description of the scattering process are

needed. We have demonstrated that a random medium can be used as a massively parallel polarimeter having a remarkable precision. This kind of polarimeter should be useful for applications (i) requiring “instantaneous” (one shot) or very high speed measurements, (ii) involving high energy pulses so long as nonlinear effects are minimal (this can be further investigated), (iii) requiring transfer of information encoded in the polarization state of light (i.e. keying with a large number of available symbols per time slot).

Unique characteristics of such scattering based device are (i) wide acceptance angle and usable waveband, (ii) the optical train does not need to be aligned with incident light, and (iii) the massively parallel measurement allows different approaches for optimizing the analysis.

4. Characterizing the fluctuations of scattered waves

The interaction of coherent electromagnetic beams with most common materials leads to a variety of specific fluctuations. As a result, the electromagnetic beams acquire usually a certain degree of randomness. The statistics of random complex fields give rise to a number of measurable distributions, including intensity, phase difference, ellipticity, and states of polarization. The most familiar occurrence of random complex fields is the family of speckle phenomena resulting from the coherent illumination of diffusive random media and scattering from rough surfaces.

A light scattering experiment in a random medium provides a wealth of information about the properties of the material under investigation. Unfortunately, the information is often too complex to process in a practical matter. For this reason, an ensemble average over several material realizations is made in order to determine the mean statistical properties of the sample. For example, coherent light that is injected into a random medium produces a speckle pattern that is indicative of the medium's specific structural properties. In order to learn anything about the global material properties, numerous speckle patterns resulting from different realizations of the material must be averaged. This averaging inherently discards "excess" information specific to particular realizations.

A random medium is typically characterized by an ensemble of realizations of disorder. When waves interact with a random medium, each member of this ensemble, i.e. each particular realization of disorder, has its own pattern of fluctuations in the scattered wave. The interaction is a non-self-averaging process, and the complicated features of the scattered waves are all rooted in the structural properties of the specific realization of randomness. In principle, the inverse problem can be solved if (i) the phase coherence is maintained over the entire interaction, (ii) the process is not dissipative, and (iii) the disorder does not vary in time. In practice, however, due to finite sizes and experimental noise, one always infringes at least on the second requirement. Furthermore, the information available is often too complex to process in a practical manner; therefore, an average over an ensemble of disorder realizations is usually taken to determine mean statistical properties. For instance, numerous speckle patterns resulting from different interactions must be averaged to learn about the global properties. Unfortunately, this averaging inherently discards information specific to particular realizations as well as the variations from one realization to the next.

As such, the following question arises: can one learn anything about the stochastic process by examining a set of its individual realizations? In principle, having access to a number of samples of the random process should allow us to study the rate of convergence toward the ensemble average characteristics. Using the example of stochastic interaction between coherent waves and random media, we will demonstrate that the significant sample to sample fluctuations can be used to extract information not available in the ensemble average. Because the convergence of the statistical properties of moments is a general problem for numerous physical phenomena that are described as random processes, concepts similar to the one discussed here may be exploited in other situations.

Let us consider the wave interaction with a random medium characterized by a number density N_v of scattering centers and by the scattering cross-section σ describing the properties of a single scattering event. For each realization of disorder α , the interaction will be defined by a specific distribution $p_\alpha(s)$ of available wave path-lengths s through the medium. When an ensemble average is taken over many such realizations, the wave interaction will be described by a probability distribution function $p(s) = \langle p_\alpha(s) \rangle = f(s, D)$ that has a universal behavior depending only on the normalized diffusion coefficient $D = 1/(N_v \sigma)$. Note that all the experimentally observable properties of the stochastic interaction can be described in terms of the probability distribution $p(s)$ whose exact functional form $f(s, D)$ may also depend on the particular geometry of an experiment. Clearly, there could be many dissimilar media with different N_v and σ that nevertheless display the same characteristics upon ensemble averaging. In practice, this ensemble can be acquired in different ways for dynamic or stationary systems, but the final result is the same: the number density and the scattering cross-section are being coupled through the diffusion coefficient, and only their product is accessible.

For a specific realization of the material disorder, however, the distribution of available path-lengths $p_\alpha(s)$ will deviate from the one corresponding to the ensemble average:

$$p_\alpha(s) = f(s, D)[1 + \delta_\alpha(s, \xi_\alpha)] \quad (26)$$

Because this deviation $\delta_\alpha(s, \xi_\alpha)$ is specific to a particular realization of disorder, it depends on variables not present in the ensemble average. Specifically, this can be expressed through a configuration function ξ_α describing the particular morphology of the given realization α . The function ξ_α describes the locations of scattering centers available in the realization and, therefore, depends only on the number density and not on the scattering cross-section. This is the reason why by examining the statistical properties of $\delta_\alpha(s, \xi_\alpha)$, one could infer information not available in the ensemble average.

Two observations about the general behavior of $\delta_\alpha(s, \xi_\alpha)$ are worth making. First, as the length s of the wave's path increases, more and more different trajectories of the same length are possible through the medium, and $p_\alpha(s)$ approaches the value corresponding to the weight of trajectories of length s in the ensemble average. In other words, in terms of the variable s , the function $\delta_\alpha(s, \xi_\alpha)$ represents a nonstationary random process. Second, because upon ensemble averaging a scattering center will exist at any position, this random function is of zero mean, $\langle \delta_\alpha(s, \xi_\alpha) \rangle = 0$ (the mean is of little practical interest). However, because of the implicit dependence on N_v , it is expected that higher order statistics of $\delta_\alpha(s, \xi_\alpha)$ can be used to reveal characteristics of the wave-matter interaction not included in the value of D .

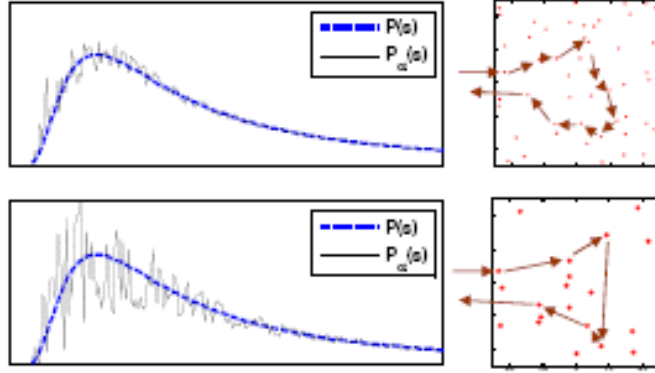


Fig 17. Sketch of path-length distributions for two media with identical mean properties (same D). The two media consist of scatterers of different cross-sections σ and different number densities N_V and are examined over the same range of path-lengths s . The medium with smaller number density provides fewer possible paths of given length s resulting in larger fluctuations of $p_\alpha(s)$.

This concept is illustrated schematically in Fig. 17 where the path-length distributions corresponding to two different media are sketched over similar ranges of s . The two media consist of scattering centers having different cross-sections but also different number densities such that, upon ensemble average, they are described by the same diffusion coefficient. Clearly, when compared to all potential trajectories, there are fewer available paths of given length s through the medium with less scattering centers. Consequently, the path-length distribution $p_\alpha(s)$ deviates more significantly from the ensemble average $p(s) = \langle p_\alpha(s) \rangle$. A measure of the nonstationary fluctuations in $p_\alpha(s)$ should discriminate between the two media, as we will show in the following.

Evidently, the random function $p_\alpha(s)$ displays not only fluctuations in s but also differences from one material realization α to another. There are many ways in which the two-dimensional statistical characteristics of $p_\alpha(s)$ can be quantified. Of course, a simple averaging over α will provide a path-length distribution $p(s) = f(s, D)$ which corresponds to the ensemble average. For a single realization α on the other hand, higher order moments of the fluctuations in $p_\alpha(s)$ can be evaluated. Even though $p_\alpha(s)$ is nonstationary in s , one can still calculate simple estimators such as, for instance, the variance $V_\alpha(\xi_\alpha) = \int \delta_\alpha^2(s, \xi_\alpha) ds - \left| \int \delta_\alpha(s, \xi_\alpha) ds \right|^2$ of the fluctuations along s . This simple estimate however is inadequate because $\delta_\alpha(s, \xi_\alpha)$ is a zero-mean random function and, consequently, a unique and meaningful normalization is difficult to define.

As the deviation $\delta_\alpha(s, \xi_\alpha)$ from the ensemble average can be regarded as a form of disorder, we can choose to examine its variance in terms of the Shannon information entropy:

$$H_\alpha(s_1, s_2) = - \int_{s_1}^{s_2} \frac{\delta_\alpha^2(s, \xi_\alpha)}{\int_{s_1}^{s_2} \delta_\alpha^2(s, \xi_\alpha) ds} \log \left(\frac{\delta_\alpha^2(s, \xi_\alpha)}{\int_{s_1}^{s_2} \delta_\alpha^2(s, \xi_\alpha) ds} \right) ds. \quad (27)$$

In Eq. (27), we define this finite scale entropy to account for realistic situations of any measurement that extends over a finite range $[s_1, s_2]$. Furthermore, the finite scale entropy can be normalized to its maximum allowable value for the entire range $S = s_2 - s_1$ as

$$h_\alpha(s_1, s_2) = -H_\alpha(s_1, s_2) / \log \left(\frac{1}{S} \right). \quad (28)$$

Of course, the normalized entropy $h_\alpha(s_1, s_2)$ will still vary from realization to realization and one can further build its average $\overline{h_\alpha(s_1, s_2)}$ over the number of realizations available. Being constructed in terms of the specific fluctuations of each realization α , this average is a comprehensive measure of the overall fluctuations in $\delta_\alpha(s, \xi_\alpha)$. It depends directly on N_v through its influence on the configuration function ξ_α .

We conducted an experiment to demonstrate that structural information not present in the ensemble average can be determined by analyzing the fluctuations in realizations of $p_\alpha(s)$. The distribution of photon path-lengths through different multiply-scattering media was measured interferometrically using the procedure of optical path-length spectroscopy (OPS)³. In OPS, the short coherence length of radiation allows selecting a specific length s of the optical paths in a manner similar to time-of-flight experiments. The OPS measurements are based on fiber optic arrangements that permit different modalities for injecting light into and collecting light from a scattering medium. The configuration can be monostatic, where the same fiber acts as both the source and detector, or bistatic when the injection and detection points are separated by an adjustable distance Δ allowing for an experimental control over the volume of interaction. In the frame of diffusion theory for lossless media, the path-length distribution $p(s, \Delta)$ corresponding to the ensemble average can be evaluated to be

$$p(s, \Delta): \exp \left(- \frac{z_e^2 + \Delta^2}{sD} \right) D^{-\frac{3}{2}} s^{-\frac{5}{2}}, \quad (29)$$

where z_e is the so-called extrapolation length.

We examined two different highly diffusive media that have approximately identical average properties. These random dielectrics are essentially non-absorbing polymer structures and have average pore sizes of 0.45 μm and 1.2 μm . Upon ensemble

³ G. Popescu, A. Dogariu, *Scattering of low coherence radiation and applications*, EUROPEAN PHYSICAL JOURNAL 32 (2): 73-93 (2005)

averaging, both are characterized by the same value of the transport mean-free path of $10 \mu\text{m}$.

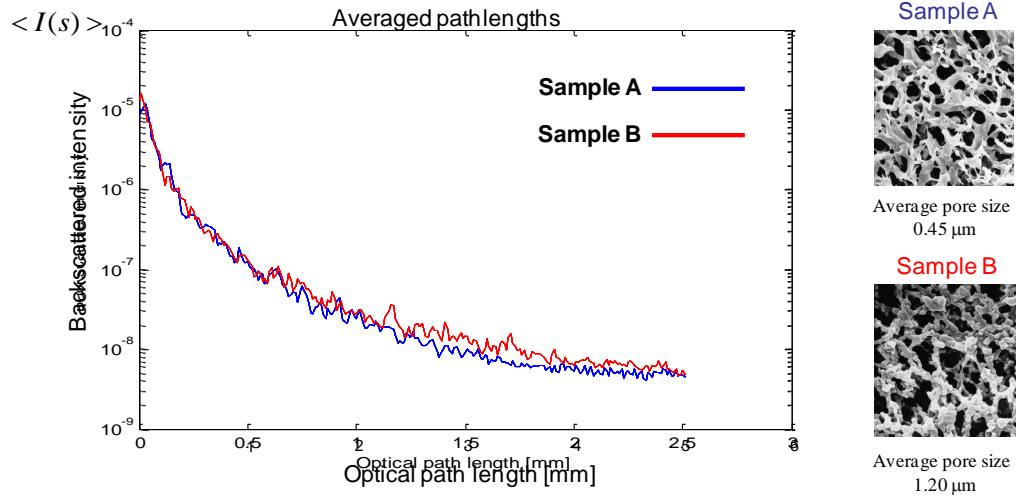


Figure 19 The averaged backscattered intensities for medium A (blue solid line) and medium B (red dashed line). The insets show typical micrographs of the materials examined.

Path-length distributions averaged over ten different realizations of these random media are shown in Fig. 19 together with their corresponding scanning electron micrographs. Even though their structural morphologies are obviously different, the similar behavior of $p(s)$ is a clear indication that, in average, the two media are being described by the same diffusion coefficient. On the other hand, the fluctuations from the average are rather dissimilar as can be seen Fig. 20 where we plot the typical mean square of the fluctuations $\delta_\alpha^2(s, \xi_\alpha)$ corresponding to the two media. In general, the medium A exhibits smaller deviations from the average which can be interpreted as a larger number of scattering trajectories available for each s . Note also that the fluctuations in $\delta_\alpha^2(s, \xi_\alpha)$ decrease for larger values of s because these random processes are nonstationary as discussed above.

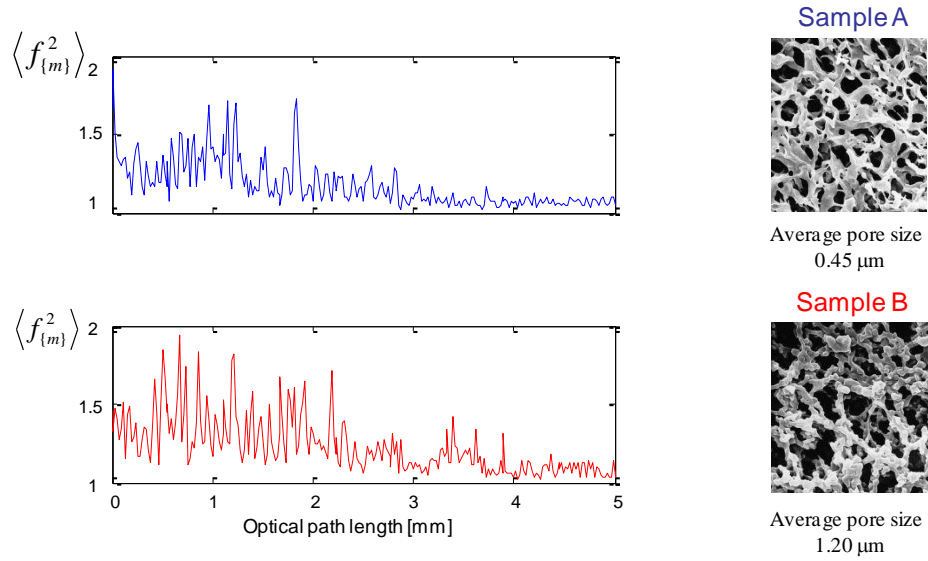


Figure 20 Typical mean square fluctuations $\delta_{\alpha}^2(s, \xi_{\alpha})$ of path-length distributions for media A and B shown in Fig.2.

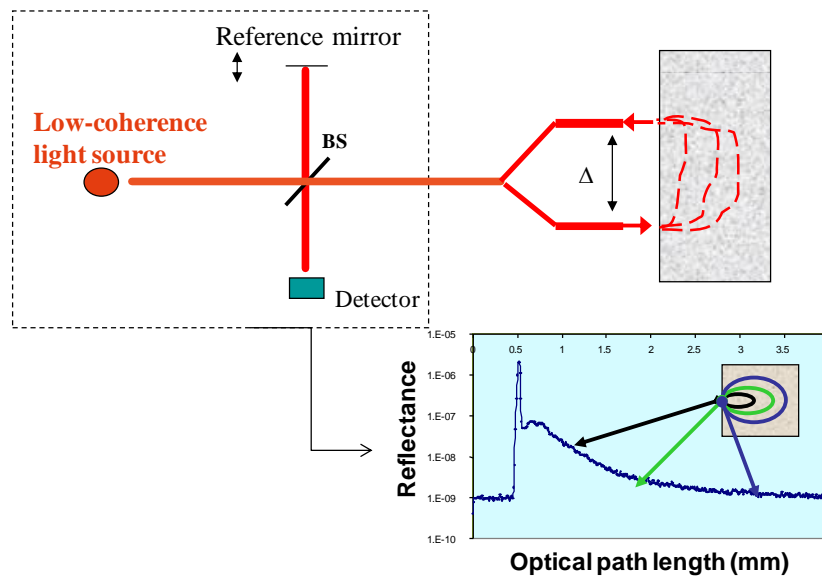


Figure 21 Typical measurement of pathlength distribution in a bistatic geometry. By increasing the source-detector separation Δ one effectively enlarges the volume of interaction with the random medium.

Let us now examine in more detail the situation where the scale of available path-lengths is varied. In practice, this amounts to controlling the size of the interaction volume which can be implemented in the bistatic OPS measurements illustrated schematically in Figure 21. By increasing the source-detector separation Δ the interaction volume is enlarged while a minimum value is enforced for a wave's paths. According to our notation, this

amounts to setting the lower path-length limit at $s_1 = \Delta$ and the upper one at $s_2 = \Delta + S$. Here S denotes the value of the total span of path-lengths available in the measurement; S is constant in our experiments. Subsequent normalization and averaging over different realizations was performed following the procedure outlined in Eq. (27).

In Fig. 22 we present the values of the normalized scale dependent entropy $\overline{h_\alpha(\Delta)}$ averaged over ten realizations of disorder for both media examined. As can be seen for both media, when the interaction volume increases, the entropy increases as expected because in all realizations α , $\delta_\alpha(s, \xi_\alpha)$ is a nonstationary process, and its fluctuations decrease at larger s . The absolute values and the rate of increase for $\overline{h_\alpha(\Delta)}$ however are medium specific.

Two main observations are in place. First, we notice the higher values of the entropy for medium A. This is the result of a higher number density N_V of scattering centers which determines a larger number of possible optical paths having a given length s . Therefore, there are smaller fluctuations in $\delta_\alpha^2(s, \xi_\alpha)$ as discussed before and, consequently, the entropy tends toward its value corresponding to an infinite number of possible trajectories of length s .

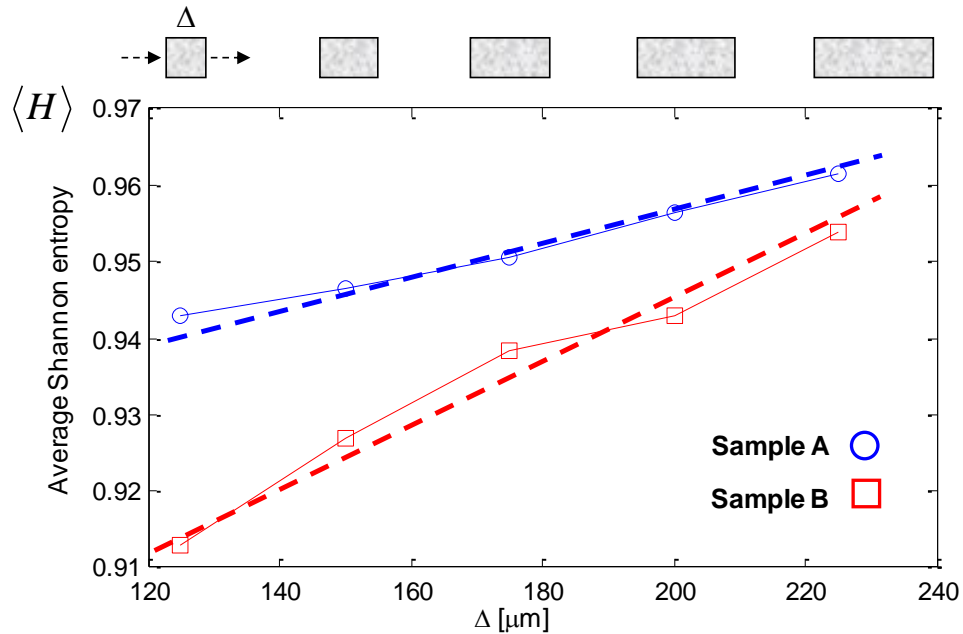


Figure 22 Average normalized entropy $\overline{h_\alpha(\Delta)}$ for medium A (blue circles) and medium B (red boxes) for increasing volumes of interaction in a bistatic configuration as depicted in the inset.

The second observation relates to the different rates of entropy increase as suggested by the dashed lines in Fig. 22. This behavior can be understood by realizing that a certain path-length s can be reached through a different number m of scattering events. For independent scattering, the joint distribution $p(s, m)$ of such a process is Poissonian and

the cumulative probability of scattering orders up to M that contribute to paths of length s is described, in average, by a universal cumulative distribution function $p(s, M)$. This cumulative distribution increases fast for low values of M and tends to saturate for higher scattering orders. In one realization where the interaction volume is finite, the maximum scattering order M contributing to a certain s is essentially determined by the number of available scattering centers. Thus, processes involving different number densities N_v will in fact experience different regions of the cumulative distribution function. For the sparser medium B, a change in M results in a faster increase of the corresponding values of $p(s, M)$ and, consequently, a faster decrease in the possible fluctuations. Because the entropy is a measure of magnitude of these fluctuations, it follows that the medium B should be characterized by a faster rate of entropy increase as can be seen in Fig. 22. As a result, in spite of being described in average by the same diffusion coefficient D , the two media can be discriminated based on the value of N_v . This information was not available in the ensemble average.

Let us now discuss the significance of these results. We have practically demonstrated a new way of analyzing the fluctuations of scattered waves resulting from the interaction between coherent fields and disordered media. In general, the complexity of such deterministic interference can be reduced only through ensemble averaging at the expense of available information. We have demonstrated that **analyzing individual members of the ensemble of interactions provides means to extract information beyond that available in the ensemble average**. This should be of particular interest for remote sensing procedures that rely on multiple exposures or extended time-scales in order to establish robust averages. In contrast to the use of statistics of steady-state interactions, the study of fluctuations in pulse propagation or interaction with finite regions of a medium open up additional possibilities. In particular, the variations from one realization of the interaction to another can provide means for target identifications or for fast detection of structural changes.

The deviation of an individual path-length distribution from the ensemble average is a nonstationary random process which also varies from one realization to another. There are different ways to analyze such a random function. Here we have shown that specific properties of the random medium's morphology can be evidenced by using the scale dependent entropy associated with the variance of path-length fluctuations. This is of particular interest in practice where the volume of interaction can be easily controlled from macroscopic to microscopic scales.

5. Polarization in randomly scattered fields

Random electromagnetic fields (REF) exist in all forms and one common origin is a result of the interaction of coherent fields with randomly inhomogeneous media. This coherent light-matter interaction is a complex interference process leading to fields with strong fluctuations in intensity. Besides their intensity fluctuations, REF are characterized by specific coherence and polarization properties.

A simple way to describe the intensity speckles is to consider the superposition of waves originating from discrete centers as a result of scattering. Different scattering regimes may vary from “single scattering” specific to most surface scattering to different degrees of multiple scattering characteristic to the interaction with three-dimensionally disordered media. When one single polarization component is analyzed, i.e. when the speckle field is measured through a polarizer, the intensity contrast often reaches unity. This is the case of the so-called fully developed speckle pattern, a manifestation of interference between a large number of wavelets with uniformly distributed random phases. This is a rather universal behavior present in scattering from a variety of media ranging from metallic rough surfaces to diffusive materials.

However, the distribution of polarization states in REF is much richer and non-universal properties are to be expected. Most importantly, it is anticipated that the polarization properties of REF corresponding to different scattering regimes will depend greatly on the strength of the scattering process. For instance, it is likely that when the wave interaction is dominated by single scattering processes, a fully developed speckle pattern will occur but the REF polarization will strongly resemble the incident state of polarization. On the other hand, when the interaction is subject to strong multiple scattering, the scattered field remains locally fully polarized but its state of polarization will vary from point to point.

5.1 Scattered fields and their intensity characteristics

A simple experiment was designed to image the REF at the surface of scattering media in a backscattering geometry. The samples were illuminated with a large, linearly polarized beam from a laser with a wavelength of 488nm and the surface was imaged onto a CCD. At the surface of the medium, the speckles are of the order of the wavelength and, in order to fully resolve them, they were magnified about ninety times to about 80 μ m in size. We used a number of sample media with varying degrees of rough surfaces and volume scattering. Figure 23 illustrates several experimentally obtained REF corresponding to a rough metallic surface (A) and three diffuse volume scattering media characterized by different transport mean free paths: a thin kaolin based diffuse coating (B), a cellulose membrane (C), and a polyvinylidene fluoride membrane (D).

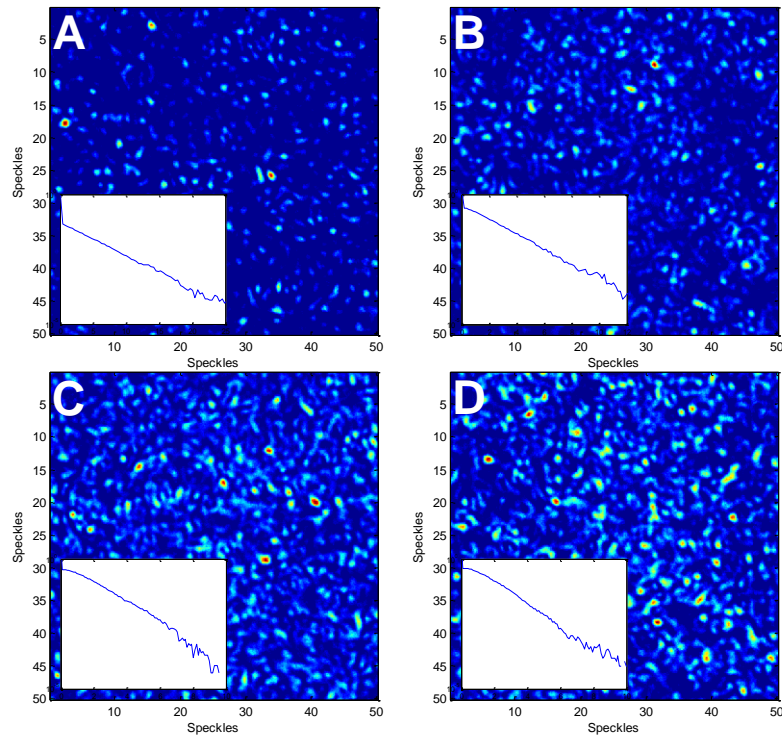


Fig. 23. Intensity patterns scattered from four different media: a rough metallic surface (A), a thin kaolin based diffuse coating (B), a cellulose membrane (C), and a polyvinylidene fluoride membrane (D). The insets show the corresponding $\log(p(I/\langle I \rangle))$ vs $I/\langle I \rangle$ distributions.

In spite of their different origins, the random fields illustrated in Figure 23 are all developed speckle patterns as demonstrated by the probability density functions of normalized intensities shown in the corresponding insets; the $p(I/\langle I \rangle)$ distributions all manifest negative exponential decays. In addition, from the intensity distributions one can evaluate the second order intensity correlations $\langle I(r)I(r+\rho) \rangle$, i.e. the average speckle size. In all cases shown, the average speckle size is approximately the wavelength of light. As such, one can conclude that both 1st and 2nd order intensity correlations are quite similar in all cases in spite of the fact that the REFs are generated by scattering on quite different random media. This means that the intensity statistics is insufficient to discriminate between REFs that are generated via different regimes of scattering.

In contrast, it is known that the polarization is more robust and resistant to random fluctuations. For instance, in single scattering from rough surfaces, the state of polarization is maintained. As the contribution of multiple scattering increases, the wave depolarizes, usually over length scales greater than the transport mean free path. Therefore, it is expected that the correlation between polarization states at the surface should be indicative of the scattering level within the random medium.

5.2 Scale dependent degree of polarization

Let us now examine the vectorial nature of the scattered fields and inspect their polarization properties. A rotating quarter-wave plate was inserted in the imaging path of the experimental setup and a subsequent Fourier analysis provided the full Stokes vector in each pixel. The spatially resolved polarimetric description of the REF can subsequently be analyzed in different ways. A common measure of polarization is the degree of polarization (DoP)

$$P(\bar{r}_i) = \sqrt{S_1^2(\bar{r}_i) + S_2^2(\bar{r}_i) + S_3^2(\bar{r}_i)} / S_0(\bar{r}_i), \quad (30)$$

$$S_1(r) = E_x^*(r)E_x(r) - E_y^*(r)E_y(r)$$

where

$$S_2(r) = E_x^*(r)E_y(r) - E_y^*(r)E_x(r) \quad . \quad (31)$$

$$S_3(r) = i(E_x^*(r)E_y(r) - E_y^*(r)E_x(r))$$

As can be seen, the DoP is actually a 4th-order field correlator describing the properties of the electric field at point r . Practically, one has access to an ensemble of different polarization states collected over a certain area and a scale dependent effective DoP can be estimated as

$$\bar{P}_A(r) = \sqrt{\int_A S_1^2 dr + \int_A S_2^2 dr + \int_A S_3^2 dr} / \int_A I dr. \quad (32)$$

The scale dependent DoP in Eq. (32) approaches zero when the ensemble of polarization states are randomly distributed over the Poincare sphere as illustrated in

Fig. 14. Of course, a strong multiple scattering interaction leads to an overall depolarized scattered field when the DoP is evaluated over a large scale. We emphasize that this depolarization only occurs in the global sense, as the resulting scattered light forms individually fully polarized speckles. The depolarization measurement can be viewed as a “center of mass” estimation, where the polarization of the average state lies within the sphere as seen in Fig 4b.

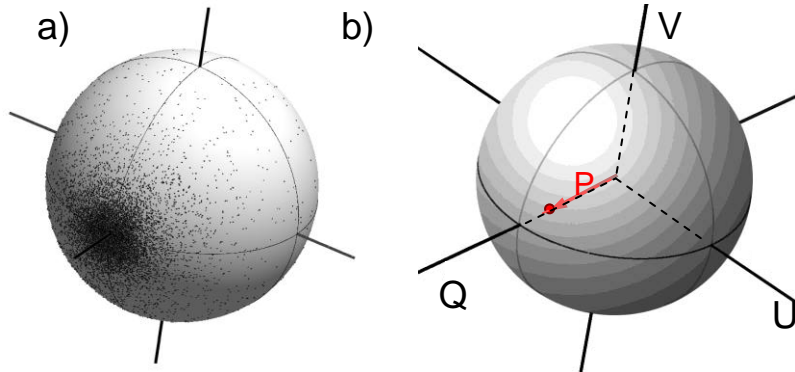


Fig. 14. a) Distribution of polarization states on the Poincare sphere. b) Both the average state of polarization and the degree of polarization are ensemble properties of the distribution of polarization states.

Results of calculations of scale-dependent DoP are presented in Fig. 25. As we increase the size of the area over which the estimation is performed, the DoP value eventually reaches saturation. The error bars in Fig 25 were calculated using one hundred starting points for each size of analysis area. Their values reflect the fact that even if each speckle is fully polarized, $\overline{P}_A(r)$ varies significantly when only examining a small number of speckles.

As evident from Fig. 25, there are two factors associated with the DoP scale dependence: the saturation level and the associated decay length. It is quite clear that the saturation levels can be quite different. For the samples illustrated here, the DoP saturation values are 0.97, 0.49, 0.32, and 0.32 +/- 0.02 for samples A, B, C, and D, respectively. Different saturation levels indicate different levels of global depolarization due to scattering: the higher the level of multiple scattering the lower the value of the corresponding degree of global polarization of the scattered field. However, the two membrane samples (C and D) show very similar DoP saturation values yet they have completely different material structures. In this case the DoP value is insufficient to discriminate between different levels of multiple scattering.

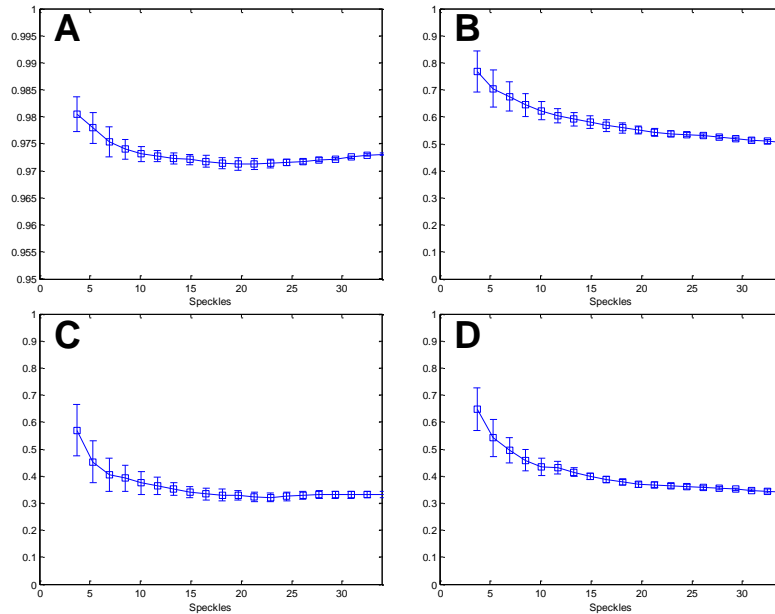


Fig. 25. The DoP calculated over an increasing integration area averaged over 100 integration centers. The error bars indicate the DoP standard deviation calculated for each integration area. Note that the y-scale in A is 0.95-1.0 while it is 0-1.0 for panels B, C, and D.

The DoP decay length represents the spatial scale at which saturation is reached. Although the media examined here have different saturations, they all have similar decay

lengths measuring about 15 intensity speckles. It appears that this decay length is an associated ensemble quantity that ignores any underlying material discrepancies.

To conclude, the DoP is a basic yet incomplete way to describe the polarization properties of REF. As mentioned before, the DoP is evaluated based on 4th-order field correlations representative for the properties of a field at one spatial location. It is also an ensemble quantity, averaged over many spatial locations, and therefore it loses any information about spatial distribution of polarization states, i.e. the shape of the distribution of states on the Poincare sphere. For instance, there are many different REF that can be characterized by the same value of the global DoP. In the following we will examine a more refined, two-point descriptor of the polarization properties of a random field.

5.3 Two point polarization correlations

Another possibility to evaluate higher-order field correlations in REF is to quantify the variability between the members of the ensemble of measurement points and a chosen reference. The measure for this is the complex degree of mutual polarization (CDMP)⁴. The magnitude of the CDMP measures the polarization similarity between two points, r_i and a reference r_0 , and under the assumption of a fully correlated and locally fully polarized field, it is defined as

$$V^2(r_i, r_0) = \frac{\left(E_x^*(r_i)E_x(r_0) + E_y^*(r_i)E_y(r_0)\right)^2}{\left(|E_x(r_i)|^2 + |E_y(r_0)|^2\right)\left(|E_x(r_i)|^2 + |E_y(r_0)|^2\right)}. \quad (33)$$

As such, CDMP measures the distance between two points (states of polarization) on the Poincare sphere; orthogonal states, opposite to each other on the Poincare sphere, have an associated CDMP value of zero. The CDMP reflects the shape of the distribution of states on the Poincare sphere in contrast to the DoP, which is a measure of the location of the center of mass of the distribution. CDMP quantifies the spatial distribution of states by comparing the Stokes vectors in each point to a common reference. Recently, similar estimations of REF properties permitted to detect local non-stationarities such as the presence of a weak localization phenomenon.

It is important to note that CDMP is not an ensemble quantity and it can be calculated while maintaining spatial information. In Fig 26 we show the spatial distribution of the REFs in Fig. 23 but this time encoded in the CDMP values calculated with respect to the constant state of polarization of the incident field.

⁴ J. Ellis and A. Dogariu, "Complex degree of mutual polarization," Opt. Lett. **29**, 536-538 (2004).

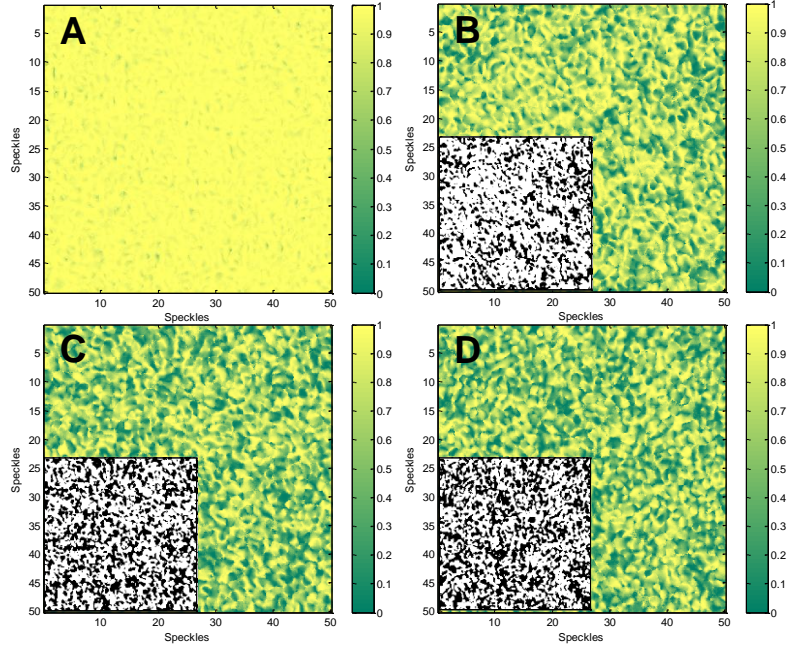


Fig. 26. CDMP maps of the REF in Fig. 1 calculated with respect to incident state of polarization. Insets show binary images of corresponding maps thresholded at $\text{CDMP}=0.5$.

As can be seen, the CDMP maps provide information about the similarity of polarization states in the REF. The rough metallic surface, sample (A), exhibits strong single scattering and as a result most of the scattered field is in the same state of polarization as the incident one; the CDMP is almost uniformly unity as a result of the strong spatial correlation of the polarization. As the level of multiple scattering increases, the spatial correlation of the CDMP maps reduces as seen for samples B, C, and D.

To assess quantitatively the differences between the CDMP maps, one can examine the probability density functions (PDF) corresponding to the distributions of CDMP values across the image. As can be seen in Fig. 27, different distributions are found for the CDMP maps shown in Fig 26. Clearly, the PDFs evolve from being peaked around unity in the case of single scattering (rough surface A) to a more uniform distribution corresponding to the higher order multiple scattering processes in volume scattering media. An interesting observation can be made in regard to samples C and D. Even though the REF scattered by these media have almost the same global degree of polarization, the PDFs of their corresponding CDMP maps are noticeably different. This can be interpreted as different coverage on the Poincare sphere corresponding to similar centers of mass. Being a local 4th-order field correlation, CDMP preserves the spatial information and distinguishes between different underlying field distributions that have similar average properties.

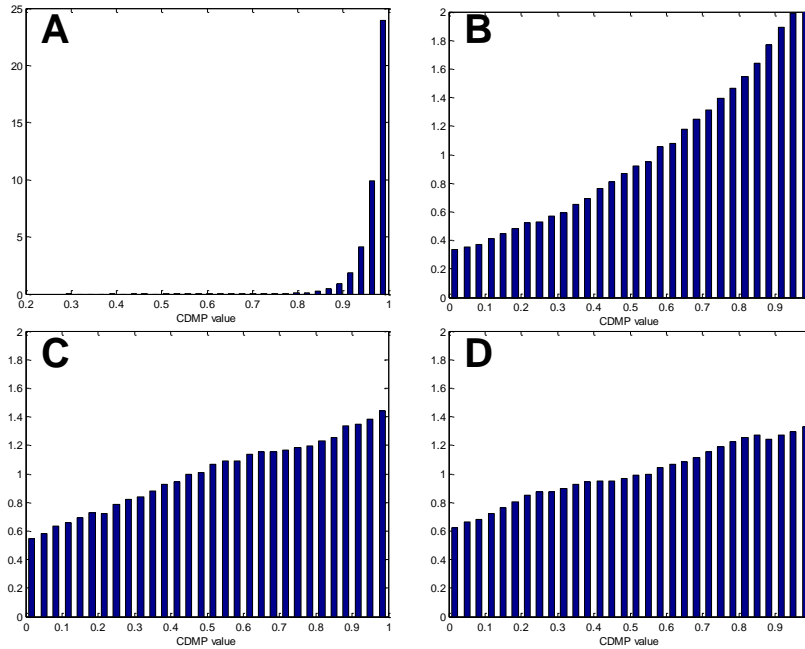


Fig. 27 Probability density functions for the CDMP distribution maps shown in Fig. 26.

We note that for a fully diffusive process of wave interaction all polarization states are equally probable and a uniform PDF is to be expected. The slight increase of the probability density towards higher CDMP values means that the diffusive scattering behavior has not been reached. In the present case this is a consequence of the backscattering geometry where the low-order scattering events are always dominant.

Let us now turn our attention to the spatial characterization of the CDMP maps in Fig. 26. As can be seen, these maps reveal areas of more uniform polarization. One can interpret these areas of spatial variation of the CDMP values as determining some sort of polarization or CDMP “speckles”. This spatial correlation over the CDMP maps is more obvious in the binary images included as insets in Fig. 26. The binary distributions were obtained by thresholding all the points having a CDMP value greater than 0.5. The field in A is clearly dominated by single scattering, where the incident state of polarization is largely maintained. In the binary images corresponding to the other samples, the different extent of clearly defined areas with similar polarization is evident, which can be understood as different levels of spatial correlations between the CDMP values. This is akin to defining an average size of the CDMP “speckle”.

When considering the distributions in the binary map shown in Fig. 26B, we found that the average size of correlated areas is about 5.3 times larger than the average size of an intensity speckle. The size of the correlation areas clearly decreases for samples C and D where it is 3.3 and 3.0 intensity speckles, respectively. Of course, the number of clusters and their size depend upon the threshold level. As the threshold decreases, the total number of points that lay above this level increases and the size of these correlated areas increases as shown in Fig. 28. However, the areas increase at different rates as clearly seen in Fig. 28, indicating different structures in the CDMP maps and, moreover, a distinctive dependence on the level of scattering in each sample. We should reiterate that

both the distribution of CDMP values in Fig. 27 and the extent of the two-dimensional CDMP correlations in Fig. 6 are obtained from one single realization of the random fields shown in Fig. 23. Thus, this analysis constitutes the point and the point-pair characterization of the polarization properties of the scattered electromagnetic field in a manner similar to the intensity distribution $p(I)$ and the average intensity-intensity correlation $\langle I(r)I(r+R) \rangle$ in a scalar speckle pattern.

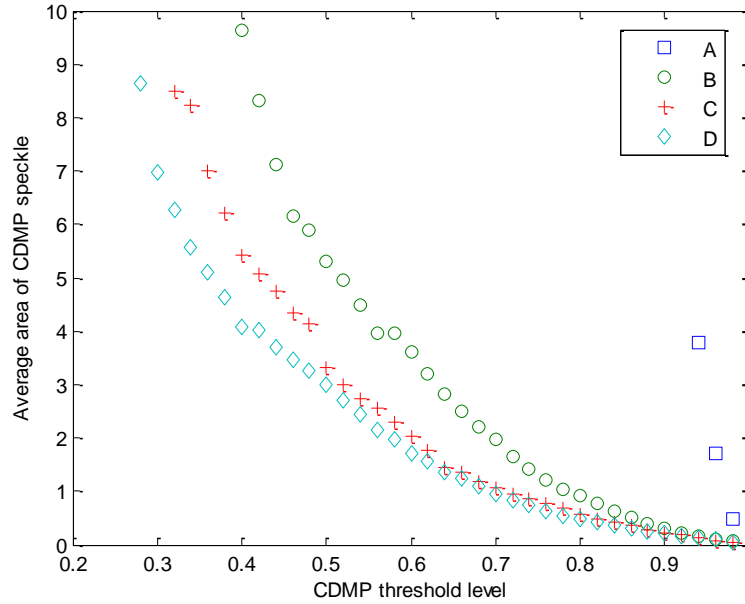


Fig. 28 Size of CDMP speckle in units of intensity speckles as a function of CDMP threshold level. Different decay rates are evident for the four samples examined.

Finally, we would like to briefly comment on the information contained in these REF properties. It is known that a number of polarization memory effects are present at different levels of scattering. There is an intimate dependence between the medium's structure and the polarimetric properties of the scattered field and, therefore, one can anticipate that the distribution of polarization states and their spatial correlation in a REF should reflect some of the morphological properties of the scattering media. Let us consider again the two samples that, in average, depolarize the light at essentially the same level, $DoP \approx 0.32$, yet their structural morphology is quite different. From Figs. 27 and 28, one can clearly see that both the PDF of the corresponding CDMP maps and the sizes of the CDMP speckles are different for these samples. This is because the structural differences lead to different scattering strengths in these two media. To assess these differences we performed typical ensemble average measurements of enhanced back scattering (EBS). These measurements yielded different values of the transport mean free path: 8 and 7 μm for media C and D, respectively, as estimated from the full width at half maximum of the enhancement peaks.

Being a measure of polarization similarity at different spatial locations, the size of the CDMP speckle reflects the extent of the interaction volume necessary for the wave to depolarize, or, in other words, to lose memory of its initial polarization state. In a specific

geometry, the magnitude of this characteristic length scale depends on the number of transport mean free paths. Therefore, scattering media characterized by small values of l^* are also expected to generate, at their surface, scattered fields with smaller values of the CDMP speckles. This is exactly what our experiments show; the lowest value of the CDMP speckle corresponds to the strongest scattering in sample D. Remarkably, one single realization of the scattering process is sufficient to provide information similar to that acquired through an ensemble average measurement.

In conclusion, we have found that the spatial variability of the vectorial properties can be markedly different even when the random fields have similar global properties. The point and point-pair correlations of the complex degree of mutual polarization provide means to identify the origins of scattered fields. We demonstrated that the extent of these spatial correlations is determined by the magnitude of the transport mean free path characterizing the scattering process. Spatially resolved measurements of the polarization properties in one realization of the scattered field allow recovering information otherwise available only through ensemble averages.

6. Unique polarization effects in scattering

One of the important features of active systems is that one can selectively probe different object characteristics by controlling the incident illumination. A possibility of interest is to structure the illuminating beams in terms of its polarization, intensity, coherence, or phase. It is expected that the structure of the illuminating field can greatly influence the information probed. For example, by illuminating a diffusive media with phase vortices of differing charge, different path-lengths are selectively probed in the enhancement peak⁵.

In order to take advantage of such unique features one has to understand the details of propagation and scattering of polarized radiation. In particular, there is a growing interest in using the specific properties of circularly polarized light (robustness in propagation, possibility of digital processing and others). Here we report on novel characteristics of scattering of circularly polarized light. These novel effects can be speculated for the design of new types of radiation sensors and for interpreting specific scattering signatures. In addition, this research may also lead to new possibilities for optical manipulation of matter.

In elastic scattering from a non absorbing spherical particle, two parameters of the electromagnetic field are conserved: the energy and the angular momentum component along the propagation direction. Linear momentum as a whole is also conserved, of course, but some of it is transferred to the particle leading to radiation pressure. The conservation of energy (which is a scalar quantity) leads to a normalization condition for the integrated energy flux density, which is further used in defining the scattering cross section. Similarly, the conservation of angular momentum should be related to the angular momentum flux density. The continuity conditions for the angular momentum density can be described by three equations (one for each component of the vector) or one equation for a tensor.

We are interested in calculating the angular moment flux density of the electromagnetic field which results from scattering of a circularly polarized wave from a non-absorbing spherical particle. It was demonstrated that scattering of circularly polarized wave does not exert torque on the particle and that transfer of angular momentum from the field to the particles is mediated only by absorption. Therefore, the angular momentum of the field is preserved and it should be interesting to know how the flux density of the angular momentum is distributed between the spin or polarization term which will be henceforth designated by \mathbf{s} and the orbital angular momentum (OAM), which will be denoted by \mathbf{l} . The total angular momentum flux density, \mathbf{j} , is given by the sum of these two terms.

⁵ Field correlations under vortex illumination have been found to act as a type of path-length filter. Furthermore, modification of the illuminating structure allows for a deterministic change in the measured field correlations, allowing for a novel and simplified means of measuring structural properties of the medium, cf. C. Schwartz and A. Dogariu, "Coherent backscattering of singular beams," *Opt. Commun* **258** (2006)

6.1 Scattering effects on spin angular momentum

Let us consider an incident plane wave which is monochromatic (angular frequency ω), left circularly polarized, has an amplitude E_0 and propagates in the direction \hat{z} (the 'hat' denotes a unit vector). This is the simplest example of a paraxial wave which has the general form

$$\mathbf{E}(x, y, z) = \exp(ikz) \mathbf{F}(x, y, z) \quad (34)$$

(where $\mathbf{F}(x, y, z)$ is a slowly varying spatial envelope). For such a wave one can employ expressions for angular momentum flux density of a paraxial wave and write the z component of the angular momentum flux density can be written as

$$\begin{aligned} j_z(x, y, z) &= \frac{c \varepsilon_0}{i2\omega} \mathbf{E}^* \left(\mathbf{r} \times \nabla \right) \mathbf{E} \Big|_z + \frac{c \varepsilon_0}{i2\omega} \mathbf{E}^* \times \mathbf{E} \Big|_z \\ &= \frac{c \varepsilon_0}{2i\omega} F_k^* \left(x \frac{\partial}{\partial y} - y \frac{\partial}{\partial x} \right) F_k + \frac{c \varepsilon_0}{2i\omega} (F_x^* F_y - F_y^* F_x). \end{aligned} \quad (35)$$

The first term relates to the transverse distribution of the field and is the OAM term. The second term reflects the angular momentum carried by circular polarization is zero for linear polarization and. For a class of paraxial beams for which the transverse field distribution can be written as

$$\mathbf{F}(r, \phi) = u(r) \exp(im\phi) \hat{F} \quad (36)$$

and recognizing that $\left(x \frac{\partial}{\partial y} - y \frac{\partial}{\partial x} \right) = \frac{\partial}{\partial \phi}$ we find that

$$j_z(r, \phi) = \frac{c \varepsilon_0}{2\omega} (m + \sigma) |u(r)|^2 = (m + \sigma) \frac{I}{\omega}. \quad (37)$$

In Eq. (37) σ is the wave helicity: +1 for left circular polarization, -1 for right circular polarization and 0 for any linear polarization. These beams are called vortex beams and they exhibit an axial singularity since the phase is indeterminate on the beam axis. Due to destructive interference, this phase singularity leads to an intensity null. The integer factor m is called the topological charge of the singularity and it is an invariant of the propagation. This follows from the fact that m relates directly to the orbital angular momentum and, under the paraxial approximation, each term of the angular momentum is conserved independently.

The flux density of the angular momentum of the incident plane wave which is carried by the spin term is equal to I_0/ω where $I_0 = \varepsilon_0 c E_0^2/2$ (ε_0 being the permittivity of vacuum and c the velocity of light). This corresponds to a quantum description in which each photon in the incident field carries a spin angular momentum of $+\hbar$. The rate at which

the angular momentum is removed from the incident field can be derived from the scattered power and is given by $\sigma_{sc} I_0 / \omega \hat{z}$. This is the source term for the angular momentum of the scattered field and it should be recovered by integrating over all directions the angular momentum flux density of the scattered field.

From general scattering theory it is known that the scattered electric field in the far zone can be written as

$$\mathbf{E}(\theta) = \begin{pmatrix} E_L(\theta) \\ E_R(\theta) \end{pmatrix} = \frac{\exp(i k r)}{r} \begin{pmatrix} S_{LL}(\theta) & S_{RL}(\theta) \\ S_{LR}(\theta) & S_{RR}(\theta) \end{pmatrix} \begin{pmatrix} E_0 \\ 0 \end{pmatrix}, \quad (38)$$

where the matrix \vec{S} is the scattering matrix in the circular polarization basis, the L and R subscripts designate the left and right circular polarizations. In Eq (38), k is the wave number and r is the distance from the center of the scattering particle which is both the origin of the coordinates frame and the reference point for the angular momentum calculations. The scattering matrix in the circular base can be related to the more usual amplitude scattering matrix given in terms of the parallel and perpendicular electric field components with respect to the scattering plane. For a spherical particle, this scattering matrix is diagonal with elements $S_2(\theta)$, $S_1(\theta)$ and the relation is

$$\begin{pmatrix} S_{LL}(\theta) & S_{RL}(\theta) \\ S_{LR}(\theta) & S_{RR}(\theta) \end{pmatrix} = \frac{1}{2} \begin{pmatrix} S_2(\theta) + S_1(\theta) & S_2(\theta) - S_1(\theta) \\ S_2(\theta) - S_1(\theta) & S_2(\theta) + S_1(\theta) \end{pmatrix}. \quad (39)$$

The scattered field can now be written as

$$\mathbf{E}(\theta, \phi) = \frac{\exp(i k r)}{r} E_0 \exp(i \phi) \left\{ S_{LL}(\theta) \hat{L} + S_{LR}(\theta) \hat{R} \right\} \quad (40)$$

and expanding further the left and right circular unit vectors in terms of the locally transverse unit vectors

$$\begin{aligned} \hat{L} &= \frac{1}{\sqrt{2}} \begin{pmatrix} \hat{\theta} + i \hat{\phi} \\ \hat{\theta} - i \hat{\phi} \end{pmatrix} \\ \hat{R} &= \frac{1}{\sqrt{2}} \begin{pmatrix} \hat{\theta} - i \hat{\phi} \\ \hat{\theta} + i \hat{\phi} \end{pmatrix} \end{aligned} \quad (41)$$

one finally obtains

$$\begin{aligned}
\mathbf{E}(\theta, \phi) &= \frac{\exp(ikr)}{r} E_0 \exp(i\phi) \frac{1}{\sqrt{2}} \left\{ [S_{LL}(\theta) + S_{LR}(\theta)] \hat{\theta} + i[S_{LL}(\theta) - S_{LR}(\theta)] \hat{\phi} \right\} \\
&= \frac{\exp(ikr)}{r} E_0 \exp(i\phi) \left[S_\theta(\theta) \hat{\theta} + S_\phi(\theta) \hat{\phi} \right],
\end{aligned} \tag{42}$$

where the notation

$$S_\theta(\theta) = [S_{LL}(\theta) + S_{LR}(\theta)]/\sqrt{2} \quad \text{and} \quad S_\phi(\theta) = i[S_{LL}(\theta) - S_{LR}(\theta)]/\sqrt{2} \quad \text{has been used.}$$

Having found \mathbf{E} , we can now proceed to calculate the angular momentum flux density through a radially oriented infinitesimal area in the radiation zone. When the wave is approximated locally as a plane wave the spin term can be found to be

$$\begin{aligned}
\mathbf{s}(\theta) &= \frac{\varepsilon_0 c}{i2\omega} \mathbf{E}_s^* \times \mathbf{E}_s = \frac{\varepsilon_0 c}{i2\omega} \frac{E_0^2}{r^2} [S_\theta^*(\theta) S_\phi(\theta) - S_\phi^*(\theta) S_\theta(\theta)] \hat{r} \\
&= \frac{\varepsilon_0 c}{2\omega} \frac{E_0^2}{r^2} [|S_{LL}(\theta)|^2 - |S_{LR}(\theta)|^2] \hat{r}.
\end{aligned} \tag{43}$$

This result is physically reasonable: the spin is simply the difference of intensities of the two radially outgoing orthogonal circular polarization components divided by the angular frequency of radiation. The common phase term $\exp(i\phi)$ does not play a roll in this calculation.

Due to axial symmetry, all the components of \mathbf{s} average to zero when an integration over the angles is performed except for the z component which is

$$s_z(\theta) = \frac{\varepsilon_0 c}{2\omega} \frac{E_0^2}{r^2} [|S_{LL}(\theta)|^2 - |S_{LR}(\theta)|^2] \cos(\theta). \tag{44}$$

For a Rayleigh scatterer, one can immediately find that the expression in Eq. (44) reduces to

$$s_z(\theta) = \frac{3\varepsilon_0 c}{16\pi\omega} \frac{E_0^2}{r^2} \sigma_{sc} \cos^2(\theta). \tag{45}$$

In order to calculate the total scattered flux, the spin flux density must be integrated over a sphere of radius r to obtain

$$\bar{s}_z = \frac{1}{4} \frac{\varepsilon_0 c}{\omega} E_0^2 \sigma_{sc} = \frac{1}{2} \sigma_{sc} \frac{I_0}{\omega}. \tag{46}$$

The bar superscript in Eq. (46) indicates integration over a sphere of arbitrary radius, in the far field. Notably, one can see that only half of the angular momentum flux removed

from the incident wave is contained in the spin term. Of course, this conclusion is similar to the results obtained for the case of a field radiated by a rotating dipole. A similar treatment can be developed for the more complex case of a Mie scatterer.

6.2 Scattering effects on orbital angular momentum

Let us now turn our attention to the more complex issue of the OAM term which is

$$\mathbf{l}(\theta) = \frac{\varepsilon_0 c}{i2\omega} \mathbf{E}^* \left(\mathbf{r} \times \nabla \right) \mathbf{E}. \quad (47)$$

In order to evaluate this expression we employ the spherical coordinates form of the gradient operator and recall that the unit vectors have to be differentiated as well; for

example $\frac{\partial \hat{\theta}}{\partial \phi} = \cos(\theta) \hat{\phi}$ and $\frac{\partial \hat{\phi}}{\partial \phi} = \left(\hat{z} \cos(\theta) - \hat{r} \right) / \sin(\theta)$. Also note that the common

phase term, $\exp(i\phi)$, is important in this case and should be considered in the differentiation. Accounting only for the terms that contribute to the z component, we obtain after some algebra that

$$l_z(\theta) = \frac{\varepsilon_0 c}{2\omega} \frac{E_0^2}{r^2} \left\{ |S_{LL}(\theta)|^2 + |S_{LR}(\theta)|^2 - \left[|S_{LL}(\theta)|^2 - |S_{LR}(\theta)|^2 \right] \cos(\theta) \right\} \quad (48)$$

This result, together with the one expressed in Eq. (46) indicate that $s_z(\theta)$ and $l_z(\theta)$ sum up to an expression which is proportional to the scattered intensity. For each θ , the total angular momentum flux density is simply the intensity divided by the angular frequency of the radiation. Integrating over a spherical surface in the far field leads indeed to a manifestation of the conservation of angular momentum flux:

$$\overline{j_z} = \overline{s_z} + \overline{l_z} = \sigma_{sc} \frac{I_0}{\omega} \hat{z}. \quad (49)$$

Moreover, we note again that at each θ , the ratio $j_z(\theta)/I(\theta)$ is constant. In the quantum description one may say that a photon scattered in any direction carries the same angular momentum as an incident photon, but, in different directions it is distributed differently between the spin and OAM terms. It is now evident that in the forward and backward directions the angular momentum is carried only by the polarization. In other words the helicity is fully preserved in the forward direction and it is fully reversed in the backward direction. For some angles, which for a Rayleigh scatterer is only 90° , on the other hand, the scattered light is linearly polarized and therefore does not carry any spin angular momentum. At these angles the angular momentum is carried only by OAM term.

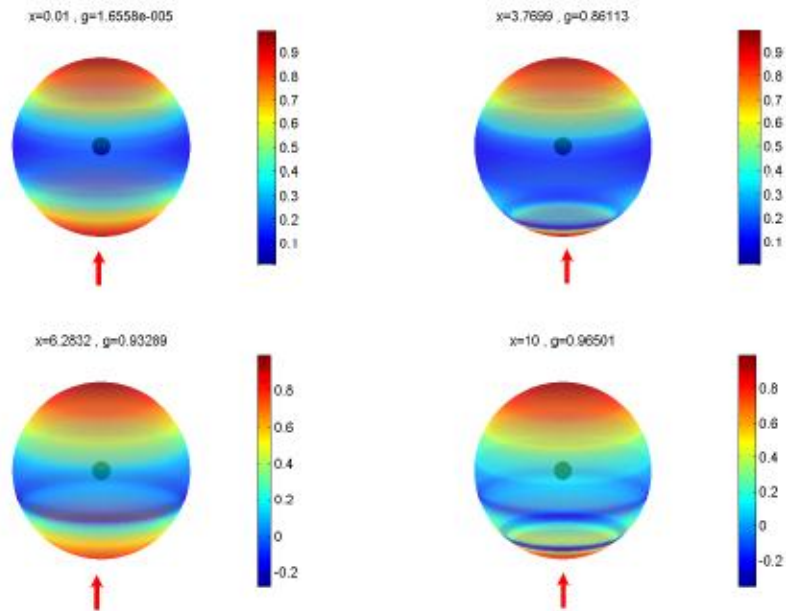


Figure 29. Three-dimensional angular distributions of the normalized spin term (angular momentum content of the spin term divided by the intensity) for several size parameters. The relative index of refraction was 1.09 . Left circularly polarized light is incident along the z axis (the direction is indicated by the red arrow). The color bars represents the spin and a complementary illustration can be obtained for the OAM

Figure 29 illustrates the three dimensional distribution of the spin term (relative to the scattered intensity) plotted as a function of scattering direction for several values of the size parameter $x = 2\pi a/\lambda$, where a is the radius of the particle and λ is the wavelength. The orbital angular momentum distribution is the complementary one (as it will be given by one minus the spin). It is interesting to note that for small size parameters the changes in the normalized distribution are small. For large particles on the other hand, in which Mie resonances are dominant, one can observe that there are directions in which the spin term is negative- meaning that the normalized orbital term is larger then 1. The transition to such behavior happens for particles with a size parameter of about π (i.e. a particle diameter which is approximately equal to the wavelength).

In order to illustrate the distinction between spin and orbital angular momenta one may use the following "gedanken" experiment. Let us consider a small dielectric sphere which is slightly absorbing, and is placed in the far field of a Rayleigh scatterer. In the exact forward direction the particle will rotate about itself due to the absorption of circularly polarized light. At of 90° with respect to the direction of incidence, on the other hand, the test particle will "orbit" the scattering particle due to the phase gradient in the scattered field. We would like to emphasize that this effect is not due to absorption and that, of course, the test particle will experience a radial force due to radiation pressure.

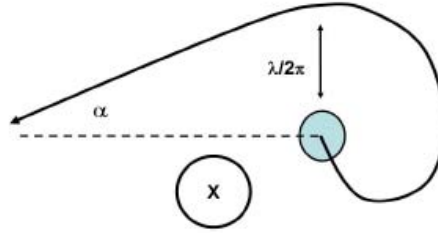


Figure 30. Qualitative illustration of the Poynting vector direction for radiation scattered by a Rayleigh scatterer illuminated by a circularly polarized light which is perpendicular to the plane of the figure as indicated. The spiraling of the Poynting vector results in an apparent angular shift of the light at the far field.

Finally, we note that the orbital angular momentum of scattered light can also be interpreted as the result of a slight direction dependant shift of the apparent origin of the scattered waves, a shift which introduces an "impact parameter" of the order of $\lambda/2\pi$. The origin of this shift can be identified in the classical electromagnetic theory where it is known that the Poynting vector of radiation from a rotating dipole (equivalent to a Rayleigh scatterer illuminated by a circularly polarized light) spirals in the near field. As a result the far field radiation seems to be emerging not from the center of the dipole but from a shifted position as illustrated qualitatively in Figure 30. The angle α is approximated by $\lambda/2\pi r$ and the angular momentum at the point \mathbf{r} can then be calculated to be $kr\alpha = 1$. This means of course that the orbital angular momentum carries all the angular momentum. In our gedanken experiment, the slight tilt of the \mathbf{k} -vector induces a rotating motion of the test particle placed at \mathbf{r} . This is the mechanism which couples angular momentum from the electromagnetic field to the medium.

6.3 Spin transport through dielectric interfaces – spin Hall effects of light

We conducted an experiment to demonstrate one important consequence of this spin-orbit interaction. As we have seen, in addition to energy and linear momentum, a light wave carries angular momentum distributed between orbital $\frac{c\epsilon_0}{i2\omega} \mathbf{E}^* (\hat{\mathbf{r}} \times \nabla) \mathbf{E}|_z$ and spin $\frac{c\epsilon_0}{i2\omega} \mathbf{E}^* \times \mathbf{E}|_z$ terms. The orbital angular momentum (OAM) term is determined by the macroscopic energy flow with respect to an arbitrary reference point and does not depend on the wave's polarization. The spin angular momentum (SAM) on the other hand, relates to the phase between orthogonal field components and is completely determined by the state of polarization. Because the total angular momentum is conserved along propagation, when a wave encounters a refractive index inhomogeneity (including interfaces between otherwise homogeneous media), a momentum transfer appears between the orbital and spin terms. This angular momentum exchange, or, in other words, the spin-orbit interaction (SOI), explains a number of polarization effects. But perhaps most attractive is that this description of electromagnetic wave propagation

provides an analogy with electron transport and related transport phenomena such as the spin Hall effect in semiconductors.

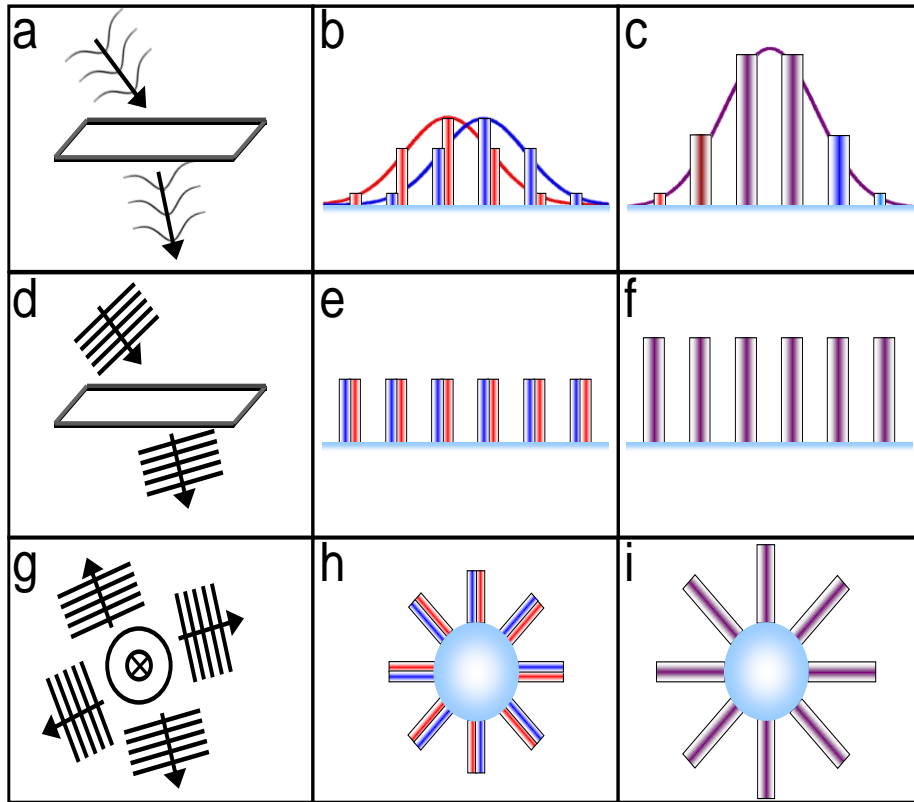


Figure 31. (a) A beam of light incident on a planar refractive index gradient, (b) beam shifts observed in far-field corresponding to incidence in pure states of polarization (right circular, left circular), and (c) the observable result corresponding to an incident beam in a mixed state. (d) A plane wave incident on a planar refractive index gradient, (e) the far-field shifts corresponding to incidence in pure states of polarization, and (f) the result of an incident plane wave in a mixed state of polarization. (g) A plane wave scattering from a sphere, (h) the transversal shifts in the perceived sphere center as observed in far-field for pure incident states, and (i) the result of scattering for incident wave in a mixed state.

There is a host of Hall-like effects in electronic systems, all dealing with transport phenomena resulting in some displacement current. Recently, it was suggested and demonstrated that an equivalent spin Hall effect of light (SHEL) exists and can be measured for a beam impinging on a dielectric interface (Fig. 31a). In SHEL, the electron spin is replaced by the wave's polarization, and the role of an applied electric field generating the electronic current is taken by the refractive index gradient. The effect is observed as a displacement of the beams carrying spin, i.e. a transversal shift in the perceived location of the interaction volume. For different incident spins, the shift is in

opposite directions, which is analogous to the induced electron spin flux perpendicular to the initial electronic current. When the incident beam is in a pure state (circularly polarized), a shift in the beam's center of mass may be observed as illustrated in Fig. 31b. Exciting with a mixed state, results in a separation of spin, where the region of overlap is still in a mixed state of polarization as suggested in Fig 31c.

We will now examine the case where a homogeneous plane wave is incident on the planar dielectric interface as depicted in Fig. 31d. Due to the infinite extent of the interaction, the transverse shift cannot be observed (Fig. 31e), as the refracted field is still an infinite plane wave and no reference point can be identified. When the incident field is not in a pure state, for example, linearly polarized, in spite of the transversal spin fluxes, there is no net photon current and therefore there will be no observable effect (Fig. 31f).

Let us now inspect cases of higher dimensionality. If the refractive index gradient is spherical and the excitation is a plane wave as illustrated in Fig. 8g, the conservation of angular momentum results in transversal spin flows tangent to the spherical surface. In this case, performing sequential excitations with pure states and using a detection scheme sensitive to the local direction of energy flow, the transversal shifts can be observed as we will show later. The presence of this shift breaks the symmetry of the field distribution relative to any plane that contains the propagation vector and the center of the sphere. In other words, the result of the interaction between circularly polarized light and a sphere depends on the incident spin: the sphere distinguishes between left and right. For excitation with a mixed state, the transversal shift that occurs cannot be directly observed because, again, there is no net transverse photon flux as in the case of plane wave impinging on a plane interface. It should be noted that the similar considerations may be applied in a cylindrical geometry. These circumstances are similar to the Corbino disk geometry in electronic systems, where counter-propagating spin currents are generated but no net electron fluxes can be detected.

This spherical geometry warrants a closer examination. It is now rather well understood that when circularly polarized light scatters from a dipole, the far-field Poynting vector \mathbf{S} makes an angle with the line of direct sight (radial vector $\boldsymbol{\rho}$). This determines a shift in the perceived position of the dipole. The shift is perpendicular to the plane of scattering, and has opposite signs for excitations with different spins as seen in Fig 32. Its value

$$\Delta_{dipole} = (\lambda/2\pi) \left[\sin \theta / (1 - 1/2 \sin^2 \theta) \right] \quad (50)$$

depends on the polar angles of scattering θ and reaches a maximum in the plane where a full transformation from SAM to OAM occurs: the plane perpendicular to the direction of propagation of the incident wave ($\theta = \pi/2$). Note that this shift does not depend on the optical properties of the scatterer. For a sphere of finite size, in the far field, the shift in perceived location is $\Delta = \lim_{\rho \rightarrow \infty} \rho (|S_{\perp}|/|S_{\rho}|)$, where S_{\perp} and S_{ρ} are the components of \mathbf{S} perpendicular and parallel to $\boldsymbol{\rho}$.

In general the transformation of SAM to OAM is not complete. However, for certain sets of parameters (sphere radius, refractive index) there are one or several angles θ where transformation is total and the scattered light is linearly polarized. The value of Δ corresponding to these angles attains local maxima and can reach tens of wavelengths in

magnitude. This modification in the perceived location of the sphere as shown in Fig. 32 is the **manifestation of the spin Hall effect** in scattering from a finite object.

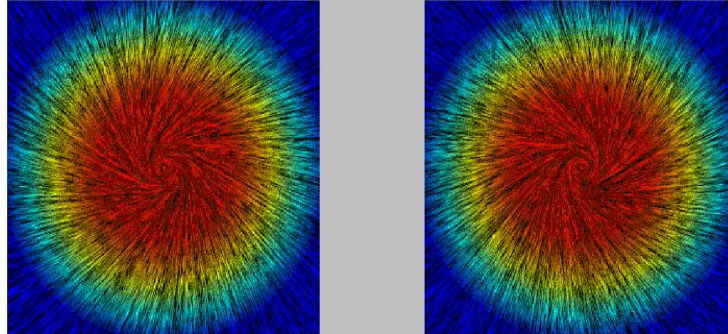


Figure 32. Poynting vector field lines for radiation scattered by a Rayleigh scatterer illuminated by left and right circularly polarized light. The spiraling of the Poynting vector results in the far-field angular shift suggested in Figure 30.

There is one feature in the scattering of circularly polarized light from a sphere that has no analog in previous descriptions of spin transport effects: Poynting vector circulation around the sphere in near and intermediate zones. Due to SAM to OAM transformation in the case of a Rayleigh scatterer, the Poynting vector propagates along conical and spiral trajectories (Fig. 33). For larger spheres, the more complicated process of scattering results in a complex, sometimes winding trajectory of \mathbf{S} .

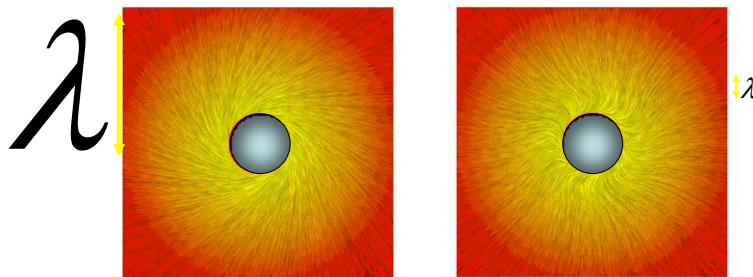


Figure 33. Poynting vector field lines projected on the plane perpendicular to the direction of excitation and containing the center of the scattering sphere. Different size spheres, smaller than the wavelength λ and larger than λ as indicated, exhibit a spiraling of the flow of energy in the intermediate region. Most interesting is the winding of Poynting vector field lines in due to the complex process of scattering from large spheres.

For instance, Fig. 33 illustrates the projection of \mathbf{S} on the plane perpendicular to the direction of excitation and containing the center of the sphere. Notably, the bending of the Poynting vector field lines as seen in Fig. 3 determines large angles between the \mathbf{S} and $\boldsymbol{\rho}$, resulting in experimentally measurable SOI effects. This intermediate zone spans up to several λ , and, therefore, an observation can be performed without significantly disturbing the field near the sphere's interface. The large intermediate zone for a sphere is due to the evanescent fields, which in this case exhibit inverse power law decay, as opposed to the exponential decay for a planar interface.

Observing the circulation of the Poynting vector in scattering from a sphere requires a detection scheme sensitive to the local energy flow. One such experiment could involve optical forces, where the trajectories of probe scatterers are analyzed in the proximity of the sphere. A much simpler procedure however can be based on a common tool having angular selectivity, i.e. a single-mode optical fiber. The coupling efficiency of a single mode fiber effectively depends on the local field distribution

$$C = \tau/2 \int_{\sigma} (\vec{E}_s \times \vec{H}^*) \cdot \hat{y} d\sigma \quad (51)$$

where E_s and H are the scattered field and fiber mode, \hat{y} is the unit vector along the fiber and τ is the electric field transmission coefficient. The integration is performed in the plane σ perpendicular to the fiber.

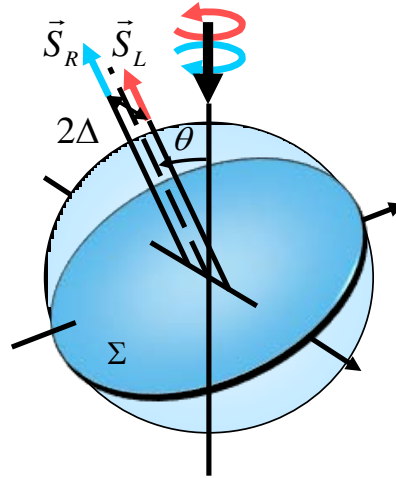


Figure 33. Due to spin-orbit interaction, a circularly polarized plane wave suffers a transversal shift Δ in any plane Σ . This shift depends on the direction of observation θ and is a manifestation of the spin Hall effect in scattering.

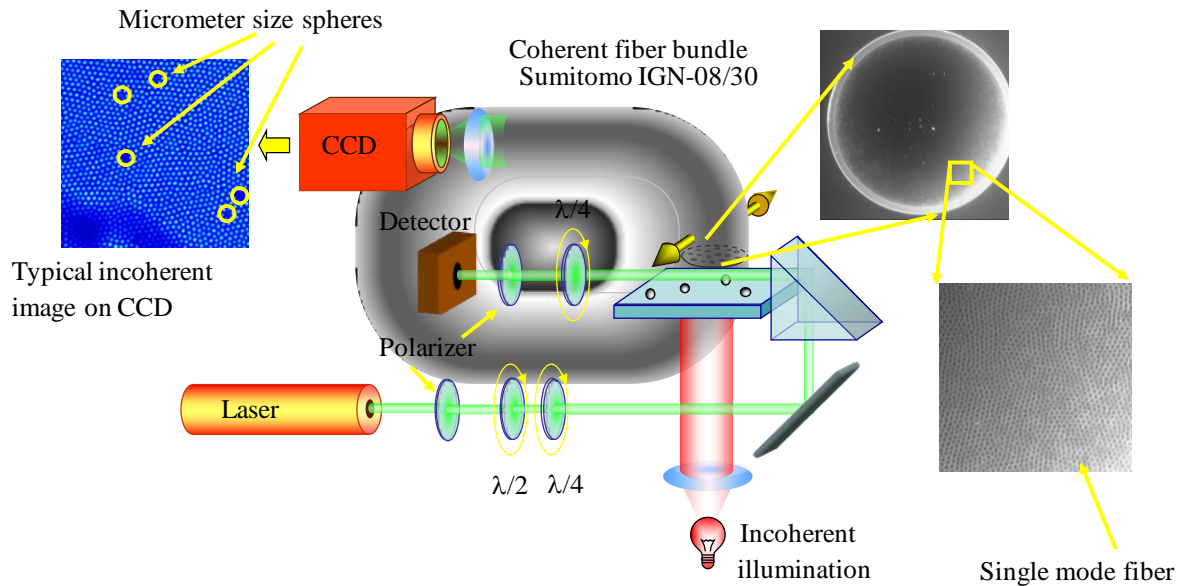


Figure 34. Schematic of the experimental setup using a single mode optical fiber as a means for sensing local power flow direction.

We used an experimental setup based on an array of single-mode optical fibers (a coherent fiber bundle) as depicted in Fig. 34. A series of measurements were performed as the fibers were scanned in the intermediate region of dielectric spheres, perpendicular to the direction of propagation of the incident field. To avoid interferences with the substrate, the spheres were suspended in oil matching the index of the microscope slide. To reveal the asymmetry in the field distribution resulting from excitation with different spins, we performed sequential measurements and recorded the corresponding scattered intensities. Subsequently, these values were subtracted to reveal the shift in the direction of \mathbf{S} .

We have also calculated analytically the intensity coupled through single-mode optical fibers after scattering from a sphere and compared them to the experimental results. The remarkable agreement is illustrated in Fig. 35 and demonstrates not only the asymmetry of the scattered fields, but also our capability to infer a shift in the perceived location of the interaction volume (sphere's location). This constitutes the first observation of transversal spin transport (a manifestation of the spin Hall effect) in scattering from finite size objects, using an object rather than the exciting field to localize the interaction.

In conclusion, due to spin-orbit interaction, an encounter with a gradient of refractive index leads to transport of spin similar to the electronic spin Hall effect. Our experiments have demonstrated that transversal spin transport is possible even when the symmetry of

optical interaction is of higher dimensionality. For a wave in a pure state of polarization, the spin-orbit interaction results in a spiraling power flow that is determined by the extent of the interaction. These results constitute the first demonstration that spin transport can be manipulated and enhanced in confined geometries, and open the possibility for developing new functionalities for sensing devices.

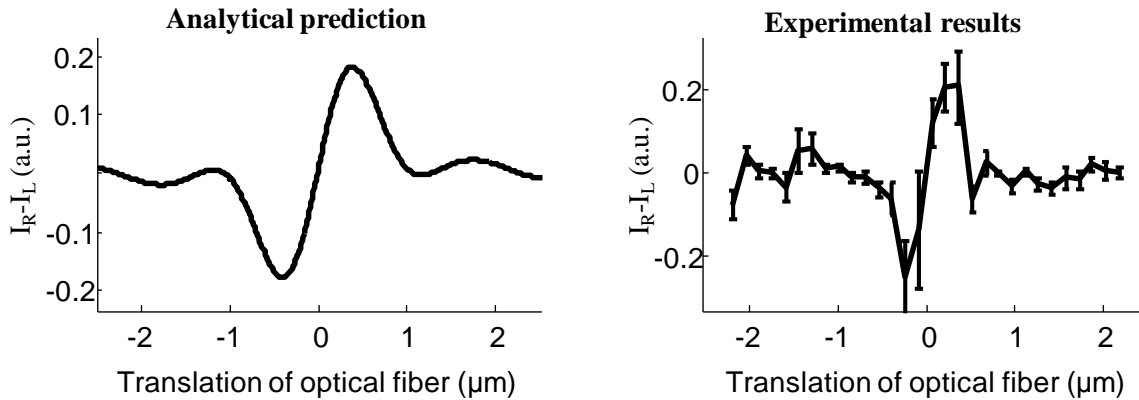


Figure 35 Comparison between the analytical prediction (a) and the experimental results (b) for the coupled power through a single mode fiber scanned across a polystyrene sphere of $4.6\mu\text{m}$ diameter. The graphs depict the difference between the scattered intensities corresponding to pure states of excitation plotted as a function of fiber's position with respect to the center of the sphere.

The significance of our demonstration is manifold. First, optical experiments are suitable tools to model spin phenomena that in electronic conduction may be difficult or even impossible to approach. This could lead to the discovery of novel manifestations of spin transport in confined geometries where effects such as loss of coherence and dissipation are expected to be minimized. Second, understanding subtle aspects of conservation laws in optical scattering should provide insights into phenomena such as spin transfer and power flow which, in turn, are essential for developing new sensing approaches at nanoscales.

Manipulating the polarization properties of electromagnetic fields may also have consequences for controlling the subwavelength behavior of optical forces. Lastly, circular polarization is rather exotic in nature and also robust in propagation. The ability to distinguish between left and right may provide unique communication channels.

7. Conservative and nonconservative optical torques

A fundamental consequence of an applied force is the ability to induce torque with respect to some reference point. Torques can also be induced by optical fields. Several concepts for optical spin motors or “*nano-rotators*” have been discussed based on optical traps created with circularly polarized light or vortex beams and relying on object’s asymmetry, absorption, or birefringence. Another notable proposal uses the subtle interplay between conservative and nonconservative forces in an optical trap to create a “*nano-fountain*” with constant circulation of trapped particles. The idea of mechanical action of light has been pursued for hundreds of years. The ability to trap and maneuver small objects such as microparticles, polymer chains, cells, etc. is undoubtedly one of the most exciting use of what is now commonly referred to as optical tweezers. A host of applications are being pursued where optical forces are employed for manipulation, measurements, or for creating and controlling new states of matter.

Two particles excited by a common field can form a bound “optical dimer” when they arrange themselves to a stable position where the radial forces acting on them are zero. We studied the canonical case of two lossless spheres that are electromagnetically coupled. Electromagnetic fields can induce conservative forces resulting from field gradients as well as nonconservative forces appearing due to radiation pressure and gradients of phase. The calculation of optical forces acting on matter is believed to be a well-established routine. The same is true for the optical forces arising in basic OB situations, even though care must be taken in describing the particle-particle interaction.

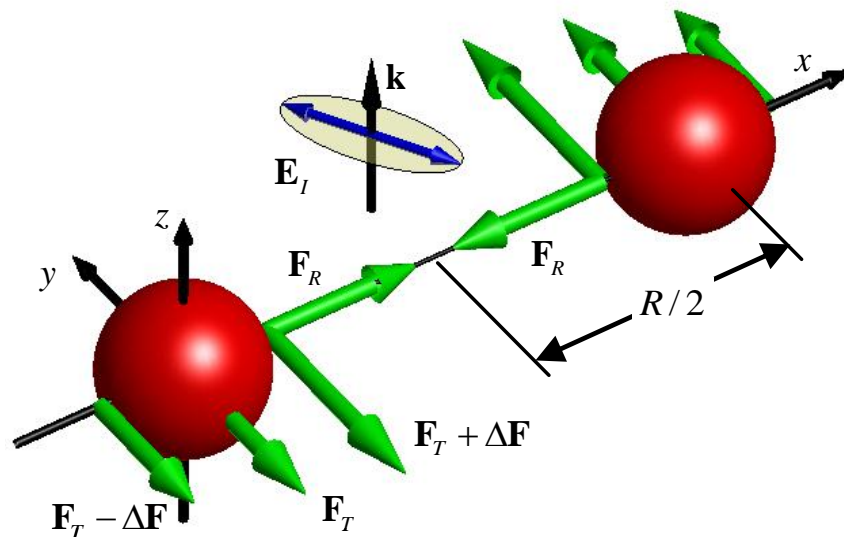


Figure 36 Optical binding in elliptically polarized light \mathbf{E}_l . Apart from the binding force \mathbf{F}_R , interacting particles experience tangential forces \mathbf{F}_T . Note the existence of differential forces $\Delta\mathbf{F}$ leading to individual spinning in addition to common orbiting of particles around the system’s center of mass.

Let us examine the system of two identical spherical particles illuminated by a plane wave propagating perpendicularly to the radius-vector connecting the centers of the particles, as shown in Figure 36. Forces are generated on the spheres due to the three-dimensional, polarized field established as a result of scattering. Due to symmetry in the x - y plane, the force acting on each particle can be decomposed into radial (binding) and tangential (rotational) components. There is also a scattering force along \mathbf{k} , but its effect is identical for the two particles and does not hamper their transversal movement.

In the simplest case of bound Rayleigh particles (dipoles), the force acting on one scatterer can be estimated as

$$\langle F_u \rangle = \frac{1}{2} \text{Re} \left(\alpha^* \mathbf{E}^* \frac{\partial \mathbf{E}}{\partial u} \right) \quad 52$$

where α is the scatterer's polarizability, \mathbf{E} is the electric field, $u = x, y, z$, and $*$ denotes complex conjugate. The field \mathbf{E} is found by solving self-consistently the system of equations that takes into account the mutual interaction between the particles

$$\begin{aligned} \mathbf{E}(\mathbf{r}_1) &= \mathbf{E}_I(\mathbf{r}_1) + \mathbf{G}\alpha\mathbf{E}(\mathbf{r}_2), \\ \mathbf{E}(\mathbf{r}_2) &= \mathbf{E}_I(\mathbf{r}_2) + \mathbf{G}\alpha\mathbf{E}(\mathbf{r}_1). \end{aligned} \quad (53)$$

In Eq. (53), \mathbf{r}_1 and \mathbf{r}_2 represent the dipole locations, $\mathbf{E}_I(\mathbf{r})$ is the incident field, and the tensor $\mathbf{G}(|\mathbf{r}_1 - \mathbf{r}_2|)$ is the inter-dipole propagator. The field derivative is then calculated to obtain the final expression for the force in Eq.(52).

A popular way for evaluating the derivative $\partial \mathbf{E} / \partial u$ is to differentiate the final solution of the system of equations (53). By doing so, however, the results contradict the calculation of time-averaged forces based on the well-established formalism of momentum flux tensor (Maxwell stress tensor). The correct way of evaluating the derivative $\partial \mathbf{E} / \partial u$ is to differentiate with respect to either \mathbf{r}_1 or \mathbf{r}_2 directly in Eq. (53). Nevertheless, it is interesting to note that the way $\partial \mathbf{E} / \partial u$ is calculated has a minor effect for the radial, binding force; this is perhaps the reason this inconsistency has not been noticed before. When evaluating the tangential forces, however, there are situations where the way the calculation of field derivatives is conducted becomes important as it will be demonstrated here.

Using Eqs. (52) and (53) one can now evaluate the radial and tangential forces to be

$$\langle F_R \rangle = \frac{|\alpha|^2}{2} \left(\frac{|E_{\parallel}^I|^2}{|1 - \lambda\alpha|^2} \text{Re} \left(\frac{\partial \lambda}{\partial r} \right) + \frac{|E_{\perp}^I|^2}{|1 - \mu\alpha|^2} \text{Re} \left(\frac{\partial \mu}{\partial r} \right) \right), \quad (54a)$$

$$\langle F_T \rangle = |\alpha|^2 \text{Re} \left(\frac{\lambda - \mu}{R} \right) \text{Re} \left(\frac{E_{\parallel}^{I*} E_{\perp}^I}{(1 - \lambda^* \alpha^*)(1 - \mu\alpha)} \right), \quad (54b)$$

where $\lambda = 2 \exp(ikR)(-ikR + 1) / R^3$, and $\mu = \exp(ikR)(k^2 R^2 + ikR - 1) / R^3$ are eigenvalues of \mathbf{G} , R is the distance between particles, and k is the wavenumber. E_{\perp}^I , E_{\parallel}^I are the components of incident field perpendicular and parallel to the separation vector. We can now proceed to examine the effect of the incident polarization.

7.1 Optical binding with linearly polarized light

Because the depth of the potential wells in the stationary points depends on the incident polarization, the system of optically bound particles tends to orient itself such that it occupies the most energetically favorable position. This may be interpreted as the result of an effective anisotropy of the system of spheres bound as a consequence of optical interaction. When the interaction is weak ($\lambda\alpha \ll 1$, $\mu\alpha \ll 1$), Eq. (54b) simplifies to $\langle F_T \rangle = |\alpha|^2 |\mathbf{E}_I|^2 \cos(2\theta) \text{Re}((\lambda - \mu)/R)$, where θ is the angle between polarization and separation vectors. We note that the tangential force varies in space proportionally to $\cos(kR)$ or $\sin(kR)$ having the same periodicity as the radial (binding) force. The tangential force acting on a dipole-like particle is zero when the field polarization is along or orthogonal to the separation vector.

For systems of larger particles there are no simple analytical results; one has to go beyond the simple dipole approximation and use numerical procedures. The method of choice is the Coupled Dipole Approximation (CDA) where a continuous volume is modeled as an array of point dipoles responding to both the excitation and mutual interactions. For modeling OB effects, we use an extension of CDA that accounts for the interaction between particles without discretizing of space between them. The calculations yield the local field distribution from which the forces acting on each individual dipoles are found. Subsequently, one may readily find the corresponding torques $\mathbf{\Gamma}_T = \sum_j \mathbf{R}_j^\perp \times \mathbf{F}_T(r_j)$ by summing over all dipoles in the system. Here \mathbf{R}_j^\perp is the component of the radius vector perpendicular to the chosen axis. In the case of OB spheres, one may identify torques resulting in two special rotational motions: (i) sphere orbiting together around their common center of mass and (ii) spheres spin about their own axis.

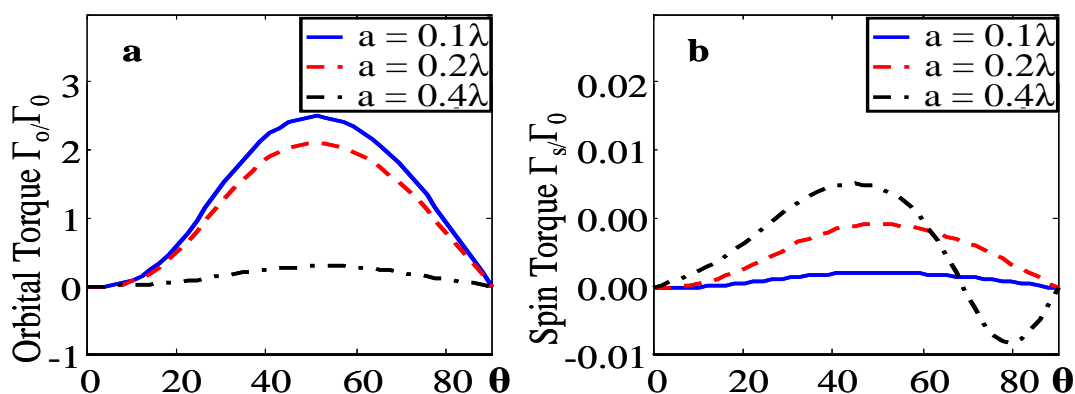


Figure 37 Torques in an optically bound system of silica spheres in water excited with a field polarized linearly at an angle θ with respect to the optical binding vector: (a) orbital torque about the system's center of mass and (b) spin torque of a sphere about its own axis. Results are shown for spheres of different sizes as indicated and the torques are normalized to $\Gamma_0 = |\mathbf{E}_I|^2 a^6 / \lambda^3$.

Typical results of CDA calculations are illustrated in Fig. 37. As can be seen, there are no torques when the incident polarization is orthogonal or along the separation vector. However, torques arise at any other angle resulting in orbital and spin motions. The unexpected appearance of spin torque is due to a gradient in the tangential force across the diameter of the spheres as shown in Fig. 36. Note that the torque does not reach its maximum for $\theta = \pi/4$ as may have been expected. The reason is that the separation vector corresponding to a stable binding position is also a function of angle θ . Another observation is that, remarkably, the spin torque can change sign for different polarization angles. In fact, the mere existence of these spin torques is a significant result, demonstrating that OB interaction can lead to rotations of lossless dielectric objects.

The torques in Fig 37 are mostly determined by gradient forces and, hence, determined by the conservative part of the total force. In any system with damping, the mechanical motion created by a conservative force will eventually cease. It follows that the OB particles will eventually align perpendicularly to the direction of polarization and that the time scales of their motion will depend heavily on the specific constraints of the damping mechanism. In the following we will reveal other situations where the nonconservative forces are the main cause for such torques, which can be controlled by the polarization of the external electromagnetic field.

7.2 Optical binding with circularly polarized light

Recently, we demonstrated that scattering of circularly polarized light from a sphere generates a spiraling energy flow around it. This effect arises from the conversion of spin angular momentum of incident light into orbital angular momentum of scattered light. One can envision that a test object placed in the vicinity of such a sphere will experience the radiation pressure from the curved power flow, causing the object to move along curled trajectory. In reality, the situation is complicated by the interaction between the two bodies as was discussed before. Moreover, together with radiation pressure, the field gradient force and the force due to gradient of phase may play a significant role. Thus, the real outcome can only be found by analyzing self-consistently the problem of electromagnetic interaction.

Starting from Eq. (3b) in the simple case of small non-absorbing dielectric particles, the tangential force can be approximated to be

$$\begin{aligned} \langle F_T \rangle = & \pm |\alpha|^2 \operatorname{Re}(\alpha) |\mathbf{E}_I|^2 [6kR(3 - k^2R^2) \cos(2kR) \\ & - (9 - 15k^2R^2 + k^4R^4) \sin(2kR)] / 4R^7. \end{aligned} \quad (55)$$

The sign is determined by the polarization's handedness. It is worth noting that the force magnitude changes as a function of R with twice the frequency compared to the optical binding force evaluated from Eq. (54a). Furthermore, contrary to the case of linear excitation, the potential landscape is now circularly symmetric as shown in the inset of Fig. 38. This means that the tangential forces are completely nonconservative and create a steady-state orbital torque about the system's center of mass. In addition to this continuous rotation around the common axis, the particles will also exhibit a continuous

rotation around their own axes due to the gradient of the nonconservative tangential force along the radial direction.

To estimate the torques acting on larger particles we used again the CDA numerical approach. A typical summary plot of the orbital torque for the first two stable bound positions is shown in Fig. 38 as function of particle radius. Also shown, are the analytical predictions of Eq. (55) for Rayleigh particles, which seem to make a good description up to a radius of about $a \approx \lambda/10$. As apparent in Fig. 38, an interesting effect occurs for larger spheres: the orbital rotation can change its sense depending on the particle size. This change in the direction of rotation, not present in the case of small particles, can happen even when moving between the different stationary orbits. Our calculations also indicate that for particles with $a \approx \lambda$, the radial and tangential forces have now similar periodicities as a function of R and, moreover, the zeros of radial force (stationary orbits) and the zeros of the tangential force occur approximately in the same place. Thus, a slight modification in the radial position of spheres can change the direction of rotation.

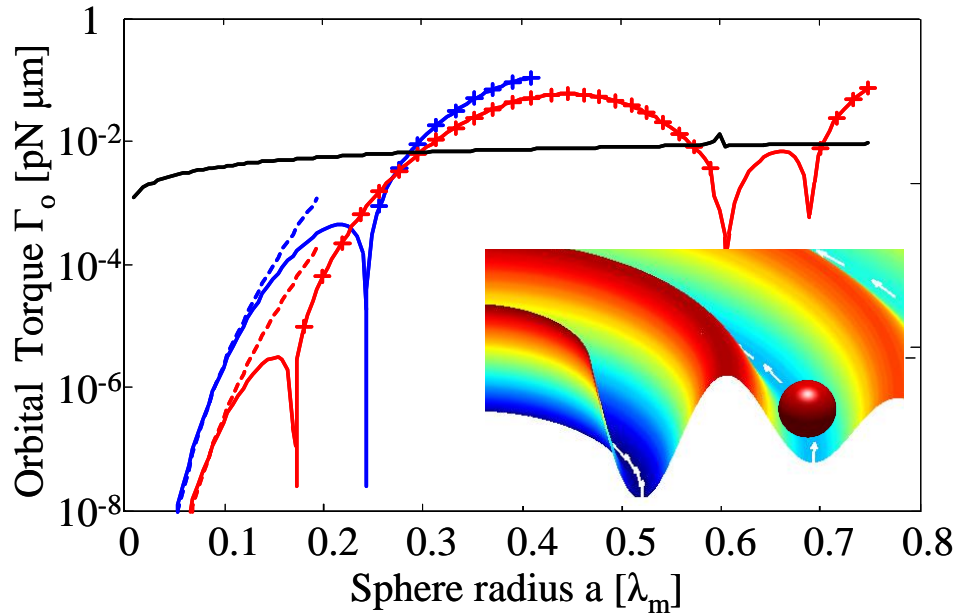


Figure 18. Magnitude of orbital torque as a function of the radius of interacting spheres for the first (blue) and second (red) stationary orbits. The plus symbols indicate regions where the torque has opposite sign. The dashed lines indicate the analytical predictions based on Eq. (55) for Rayleigh particles. The calculations are for silica spheres in water excited with a plane wave of intensity $10mW/\mu m^2$. The black line shows the magnitude of torque due to Brownian force at 290K. The inset depicts the symmetric potential energy landscape and the trajectory of a bound particle due to nonconservative orbital torques.

In addition to electromagnetic interaction, OB systems can also be subject to environmental effects. In fluids for example, the tangential force is compensated by the viscous Stokes force which, for spherical particles, is $F_s = 6\pi\eta av$, where η and v are the dynamic viscosity and the particle velocity, respectively. For particles of radius $a = 0.41\lambda_m$, for instance, the values for orbital torques in Figure 18 can be used to show

that maximal angular velocity is $\Omega_o = 2v/R \approx 3.7 \text{ rad/s}$ in the first stationary orbit. This angular velocity is easily detectable experimentally.

Another experimental aspect is Brownian motion. Directional motion due to optical forces will be affected by the additional chaotic movement associated with some random force $\langle F_B^2 \rangle = 12\pi\eta ak_B T$. The torque resulting from the Brownian force provides a useful reference for the magnitude of orbital torques. In Figure 18, one can clearly see that for $a \geq 0.3\lambda_m$ and an optical intensity of $10 \text{ mW}/\mu\text{m}^2$, the optically induced torques dominate.

Due to the complex interaction, the OB particles are also subject to spin torque with respect to the individual axes as shown in Figure 39. As can be seen, for the chosen parameters, the spin torque increases with the particle size but, similar to the orbital torque, the sense of rotation is not always the same. Examining the two types of torques in Figs. 3 and 4, one can see that the spin and orbital torques have the same direction for small particles but their behavior becomes more complicated when the sizes increase.

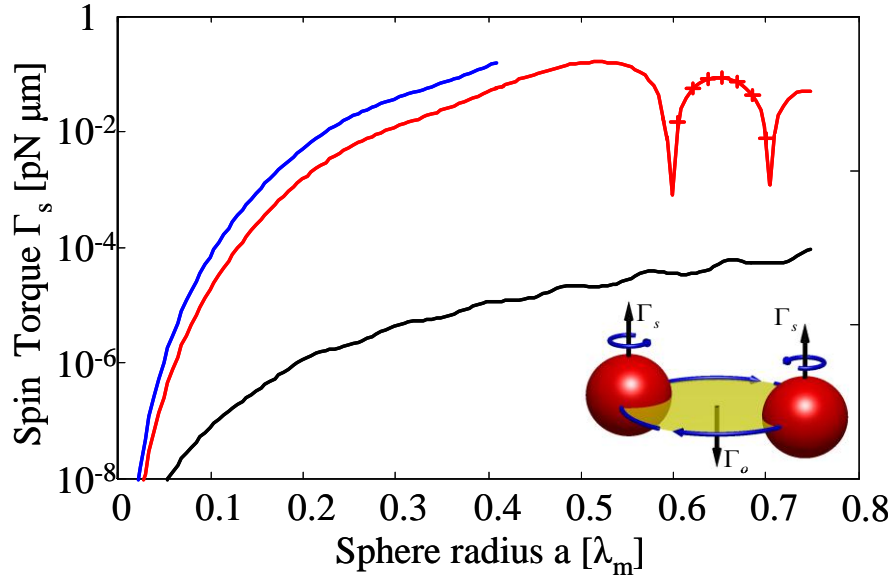


Figure 39 Magnitude of spin torque Γ_s as a function of the radius of interacting spheres for the first (blue) and second (red) stationary orbits. The plus symbols indicate regions where the torque has opposite sign. The calculations are for silica spheres in water excited with a plane wave of intensity $10 \text{ mW}/\mu\text{m}^2$. The black line shows the magnitude of absorption-induced spin torque of one silica sphere with refractive index $n_i = 1.59 + 10^{-7}i$.

Circular polarization can induce torques on a small object due to asymmetry, absorption or birefringence. Therefore, it is instructive to compare the magnitude of OB spin torque with the optical torque exerted on a particle due to its intrinsic absorption. The later can be estimated as $\Gamma_{abs} = |E_I|^2 a^2 Q_{abs}/4k$ [1], where Q_{abs} is the absorption coefficient.

Estimations based on typical values for absorption in silica are shown in Fig. 4, and, as can be seen, spin torque dominates for the entire range of particle sizes. Notably, because the OB spin torque does not necessarily have the same direction as the excitation handedness while the torque due to absorption is always in the same direction, the two torques can combine to increase or to cancel the net rotation. Our calculations show that for these two types of torques to have similar magnitudes, the imaginary part of the refractive index should be on the order of 10^{-3} . Finally, one can estimate the typical angular speeds Ω_s of spinning using the fact that the torque imparted to a rotating sphere by surrounding viscous liquid is defined as $\Gamma_v = -8\pi\eta a^3\Omega_s$. For a sphere of radius $a = 0.41\lambda_m$ and an intensity of $10mW/\mu m^2$ one finds that the corresponding spin angular velocity in water is $\Omega_s = \Gamma_s/8\pi\eta a^3 \approx 32rad/s$.

These results constitute the first demonstration that optical interaction forces can lead not only to binding, but also to complex rotations. The interplay between conservative and nonconservative forces constitutes a new mechanism to induce torques on spherically symmetric, optically isotropic, and lossless objects.

We have found that when the incident field is linearly polarized, the torques are mostly conservative and affect only the transient behaviors. For circular polarization on the other hand, the nonconservative torques are significant and lead to nontrivial phenomena. In particular, we have shown that bound systems can rotate not only around the common center of but also around their own axes. In the intermediate case of elliptically polarized light, the conservative torque will determine a transient orbital motion, whereas the nonconservative one will lead to a continuous spin rotation. The whole system can be seen as a ‘nano-mixer’ with complex mutual rotations of constituents. The direction and speed of these rotations can be dynamically controlled through the intensity, state of polarization, and spatial profile of the incident radiation. Our estimations indicate that effects are easily observable under reasonable environmental conditions. Finally, the bound system discussed here constitutes a new kind of “optical matter” having its mechanical properties strongly coupled to the exciting radiation.

8. Peer-reviewed publications with partial support from this program

Peer reviewed journal publications:

1. S. Sukhov, D. Haefner, and A. Dogariu Coupled dipole method for modeling optical properties of large-scale random media, **Phys. Rev E** **77**, 066709 (2008)
2. T. Kohlgraf-Owens, and A. Dogariu, “Finding the field transfer matrix of scattering media”, **Opt. Exp.** **77**, 13225 (2008)
3. J. Broky, K. M. Douglass, J. Ellis, and A. Dogariu , “*Fluctuations of scattered waves: going beyond the ensemble average* ”, **Opt. Exp.** **17**, 10466-10471 (2009)
4. D. Haefner, S. Sukhov, and A. Dogariu, “*Spin Hall effect in spherical geometry*”, **Phys. Rev. Lett.** **102**, 123903 (2009)
5. D. Haefner, S. Sukhov, and A. Dogariu “*Conservative and Nonconservative Torques in Optical Binding*”, **Phys. Rev. Lett.** **103**, 173602 (2009)
6. D. Haefner, S. Sukhov, and A. Dogariu, “*Scale-dependent anisotropic polarizability in mesoscopic structures*”, **Phys. Rev E** **81**, 016609 (2010)
7. J. Broky and A. Dogariu , “*Complex degree of mutual polarization in randomly scattered fields*”, **Opt. Exp.** **187**, 20105 (2010)

9. Presentations with partial support from this program

1. S. Sukhov, D. Haefner, and A. Dogariu, *Scattered intensity fluctuations for characterizing inhomogeneous media*, OSA Annual Meeting, San Jose (2007)
2. D. Haefner, J. Ellis, S. Sukhov, and A. Dogariu, *Determining Anisotropic Polarizability of Optically Inhomogeneous Media in near-field measurements* OSA Annual meeting, San Jose 2007.
3. S. Sukhov, D. Haefner, and A. Dogariu, *Scattered Intensity Fluctuations for Characterizing Inhomogeneous media*, OSA Annual meeting, San Jose 2007.
4. S. Sukhov, S. Moiseev, and A. Dogariu, *Metal-dielectric composites with dissipative and active components*, OSA Annual Meeting, San Jose (2007)
5. D. Haefner, S. Sukhov, and A. Dogariu, “*Near-Field Stochastic Scattering Polarimetry*”, 10th International Conference on Near-Field Optics, Buenos Aires, (2008)

6. D. Haefner, S. Sukhov, and A. Dogariu, “*Conservation of Angular Momentum In Mie Scattering*”, 10th International Conference on Near-Field Optics, Buenos Aires, (2008)
7. S. Sukhov, D. Haefner, and A. Dogariu, “*Effective Anisotropic Polarizability Of Random Media*”, 10th International Conference on Near-Field Optics, Buenos Aires, (2008)
8. S. Sukhov, D. Haefner, and A. Dogariu, “*Reconstructing The Local Dielectric Tensor From Near-Field Measurements*”, 10th International Conference on Near-Field Optics, Buenos Aires, (2008)
9. A. Dogariu, *Stochastic sensing at subwavelength scales*, invited lecture, University of Colorado, Boulder, (2008).
10. A. Dogariu, *Variable coherence sensing*, invited lecture, Duke University, (2008)
11. A. Dogariu, *Variable coherence for sensing applications*, invited lecture, AFRL Workshop on waves in complex media, Yountville, (2009)
12. John Broky, Jeremy Ellis, Aristide Dogariu, *Identifying Non-Stationarities in Random EM fields: Are Speckles Really Disturbing?*, OSA Annual Meeting, Rochester, (2008)
13. John Broky, Jeremy Ellis, Kyle Douglass, Aristide Dogariu, *Statistical Fluctuations: Going Beyond the Ensemble Average*, OSA Annual Meeting, Rochester, (2008)
14. David P. Haefner, Sergey Sukhov, Aristide Dogariu, *Conservation of Angular Momentum in Mie Scattering*, OSA Annual Meeting, Rochester, (2008)
15. David P. Haefner, Sergey Sukhov, Aristide Dogariu, *Near-Field Modeling of Particle-Particle Interactions*, OSA Annual Meeting, Rochester, (2008)
16. Thomas Kohlgraf-Owens, Aristide Dogariu, *Disordered Media as Efficient Optical Devices*, OSA Annual Meeting, Rochester, (2008)
17. David P. Haefner, Sergey Sukhov, Aristide Dogariu, *Local Anisotropic Polarizability in Mesoscopic Structures*, CLEO/IQEC (2009)
18. Sergey Sukhov, David P. Haefner, Girish Agarwal and Aristide Dogariu, *Enhanced Birefringence of Inhomogeneous Slabs*, CLEO/IQEC (2009)
19. Thomas W. Kohlgraf-Owens, Aristide Dogariu, *Optimized polarimetry with massively parallel polarization sampling*, SPIE Defense, Orlando (2009)
20. A. Dogariu, *Optical forces and torques at nanoscales*, invited lecture, Max Planck Institute for the Science of Light, Nov 2009.
21. A. Dogariu *Task oriented sensing with complex waveforms*, invited presentation at OSA Annual Meeting, San Jose, Oct. 2009

22. David Haefner, Sergey Sukhov, Aristide Dogariu, *Nonconservative Optical Torques*, CLEO/IQEC, San Jose, (2010)
23. Kyle M. Douglass, Gabriel Biener, Sergey Sukhov, Aristide Dogariu, *Rotational Stochastic Resonance*, CLEO/IQEC, San Jose, (2010)

Certain results of this program have also been part the PhD thesis entitled *Near-field optical interactions and applications* (2010) by Dr. David Haefner, currently with the Night Vision Army Laboratories.
